Revision 1

Hexagonal magnetite in Algoma-type banded iron formations of the ca. 2.52 Ga Baizhiyan Formation (Wutai Group, North China): evidence for a green rust precursor?

LONGFEI SUN[1, 2], MAXWELL LECHTE[3], XIAOYING SHI[1, 2], XIQIANG ZHOU[4, 5], LIMIN ZHOU[6], HAO FANG[2], BAOZENG XIE[2], MENGTING WU[7], AND DONGJIE TANG*[1, 7]

[1]State Key Laboratory of Biogeology and Environmental Geology, China University of Geosciences (Beijing), Beijing 100083, China

[2]School of Earth Sciences and Resources, China University of Geosciences (Beijing), Beijing 100083, China

[3]Department of Earth and Planetary Sciences, McGill University, 3450 University Street, Montréal, QC H3A 0E8, Canada

[4]Key Laboratory of Cenozoic Geology and Environment, Institute of Geology and Geophysics, Chinese Academy of Sciences, Beijing 100029, China;

[5]University of Chinese Academy of Sciences, Beijing 100049, China

[6]National Research Center of Geoanalysis, Beijing 100037, China

[7]Institute of Earth Sciences, China University of Geosciences (Beijing), Beijing 100083, China

*Corresponding author. E-mail: dongjtang@126.com (D. Tang), Tel.: +86 10 82323199.

ABSTRACT

Banded iron formations (BIFs) are iron-rich marine chemical sedimentary rocks, and their

mineralogy and geochemistry can be used to gain insights into ancient ocean chemistry and biospheric evolution. Magnetite is the major iron-bearing mineral in many BIFs (particularly in the Archean), and is variably interpreted to be of primary, early diagenetic or metamorphic origin. Different genetic interpretations for magnetite lead to divergent pictures of the Precambrian Earth system and its evolutionary models through time. The Baizhiyan Formation of the Neoarchean Wutai Group (Shanxi, North China) features magnetite-bearing, Algoma-type BIFs deposited ca. 2.52 Ga, in the lead-up to a major period of global iron formation deposition in the Paleoproterozoic. Abundant magnetite crystals found in the silica-rich bands of these BIFs show euhedral, hexagonal morphology. We suggest that this hexagonal magnetite likely represents pseudomorphs after green rust, a mixed-valence iron hydroxy-salt formed in the water column. The rare earth element composition of the BIFs shows negligible to slightly positive Ce anomalies ($Ce_{SN}/Ce_{SN}^* = 1.03 \pm 0.07$), which is characteristic of a dominantly anoxic water column. The presence of positive Eu anomalies ($Eu_{SN}/Eu_{SN}^* < 3.9$) suggests a substantial influence from proximal hydrothermal fluids. The co-occurrence of siderite layers associated with the magnetite-bearing strata may indicate iron cycling associated with ferruginous bottom seawater conditions. The geochemical signatures of the Baizhiyan BIFs are consistent with the interpretation that the magnetite transformed from metastable green rust. This green rust could have formed via several processes, including the partial oxidation of Fe(II) by molecular oxygen/photoferrotrophs, the reaction of settling ferrihydrite with Fe(II)-rich hydrothermal fluids under anoxic conditions, or local dissimilatory iron reduction. In all cases, the contribution of primary green rust to BIF formation requires iron redox cycling and similar pseudomorphs in the form of hexagonal magnetite may be more common in the geological record. Our findings support models in which green rust was an important primary constituent of the Precambrian iron

cycle, and the potential interactions of green rust with other elements (e.g., phosphorus) should be taken into consideration when reconstructing Precambrian biogeochemical cycles.

Keywords: ferrihydrite, iron redox cycling, ferruginous, Ce anomalies, Eu anomalies, hydrothermal fluid activity

INTRODUCTION

Iron formations (IFs) are chemical sedimentary rocks commonly made up of alternating bands of iron-rich (~15–40 wt% Fe) and silica-rich (~40–60 wt% SiO_2) minerals (Trendall 2002; Simonson et al. 2003; Klein 2005; Beukes and Gutzmer 2008; Fischer and Knoll 2009; Posth et al. 2013a; Bekker et al. 2014; Konhauser et al. 2017; Rasmussen and Muhling 2018). The vast majority of IFs were deposited in the Neoarchean and Paleoproterozoic oceans between 2.80 and 1.85 Ga (Isley and Abbott 1999), and with the exception of an episode of global IF deposition during the Neoproterozoic ice ages (e.g., Cox et al. 2016). IFs are near-exclusively deposited prior to ca. 1.85 Ga (Konhauser et al. 2017 and references therein). Based on their sedimentology, IFs are subdivided into banded iron formations (BIFs) which are composed of finely laminated iron and silica bands and generally lack wave-influenced sedimentary structures, and granular iron formations (GIFs) which are comprised thick-bedded, coarsely grained iron-rich deposits that feature evidence for shallow water deposition (e.g., Simonson 1985; Bekker et al. 2014). Iron formations that are interpreted to have been deposited in volcanic arc and rift zone settings are referred to as Algoma-type (Gross 1983). Algoma-type IFs commonly occur in greenstone belts, with limited lateral distribution (commonly less than 10 km) and thickness (commonly less than 50 m), and are associated with submarine-emplaced volcanic rocks and occasionally with volcanogenic massive sulfide deposits (Ohmoto 2003; Bekker et al. 2010). In contrast, the

Superior-type IFs are interpreted to have formed on continental shelves with a much more extensive distribution (in places greater than 100,000 km^2) (Morris 1993; Isley and Abbott 1999).

Since BIFs are chemical precipitates that have typically experienced minimal detrital input during their deposition (indicated by low concentrations of Al_2O_3 and other elements considered to be proxies for detrital input: e.g., Ti, Zr, Th, Hf and Sc), they are widely interpreted as significant archives of authigenic iron cycling (Konhauser et al. 2017). However, the primary mineralogy of BIFs remains debated, and has variously been proposed to be ferric hydroxides (i.e., ferrihydrite; e.g., Konhauser et al. 2002; Kappler et al. 2005; Sun et al. 2015; Sun and Li 2017), a Fe(III)-Si gel (e.g., Percak-Dennett et al. 2011; Zheng et al. 2016), ferrous silicates (e.g., greenalite; Eugster and Chou 1973; Rasmussen et al. 2013; Tosca et al. 2016), ferrous carbonates (e.g., siderite; Tice and Lowe 2004; Pecoits et al. 2009), mixed valence iron oxides (e.g., magnetite and green rust; Li et al. 2017; Halevy et al. 2017; Bauer et al. 2020), or combination of different phases (cf. Konhauser et al. 2017; Rasmussen and Muhling 2018). These different interpretations of the original mineralogy have distinct implications for seawater redox conditions and iron-cycling processes. Because mobile iron is required for IF genesis, if the original precipitates are ferric phases (such as ferrihydrite), then the redox cycling of iron in the water column needs to be invoked (e.g., Sun et al. 2015; Konhauser et al. 2017; Sun and Li 2017). Conversely, if the original precipitates are ferrous phases (such as greenalite), then the redox cycling of iron in the water column will not be required for the deposition of IF (e.g., Rasmussen et al. 2017). Thus, it is important to identify the original minerals in IFs, but this can be a challenging task due to potentially complex histories of diagenesis, metamorphism, deformation, weathering and hydrothermal alteration (cf., Rasmussen and Muhling 2018).

Magnetite is a mixed-valence oxide of the spinel group and is one of the major iron-rich

93 minerals in many IFs (Klein 2005), being very common in Neoarchean and older IFs, but less
94 common in latter (Li et al. 2017). The origin of magnetite in IF is highly debated, and three
95 major models have been proposed: (1) a metamorphic model, in which magnetite is interpreted
96 to be formed by the transformation of hematite, siderite or other ferrous phases during
97 metamorphism (e.g., Ayers 1972; Perry et al. 1973; Klein 2005; Köhler et al. 2013; Posth et al.
98 2013b), (2) a diagenetic model, where magnetite is produced during the bacterial reduction of
99 ferric (oxyhydr)oxides coupled with organic matter oxidation (Bell et al. 1987; Johnson et al.
100 2003; Pecoits et al. 2009; Heimann et al. 2010; Li et al. 2013a, 2013b; Konhauser et al. 2017),
101 and (3) a primary to early diagenetic model, in which magnetite either forms via the reaction of
102 biologically reactive Fe(III) mineral phases with Fe(II) during settling in an anoxic water column
103 (e.g., Usman et al. 2012a; Bauer et al. 2020), or is transformed from metastable, primary green
104 rust (mixed-valence, layered double hydroxide minerals; Halevy et al. 2017; Li et al. 2017).
105 These different interpretations for the origin of magnetite give rise to divergent pictures of the
106 Precambrian Earth system and its evolutionary models through time. It would have important
107 implications for the redox state and nutrient cycling of the ferruginous oceans if the formation of
108 primary to early diagenetic magnetite was a widespread process (e.g., Li et al. 2017; Halevy et al.
109 2017; Bauer et al. 2020). Conversely, if the magnetite is demonstrably of late diagenetic or
110 metamorphic origin, then magnetite in IFs does not directly archive the oceanic or atmospheric
111 chemical conditions (Posth et al. 2013b).

112 Petrographic evidence for metamorphic (e.g., Perry et al. 1973; Rasmussen and Muhling
113 2018) and early diagenetic magnetites (e.g., Konhauser et al. 2005; Johnson et al. 2008a) has
114 been well documented, but evidence for primary to very early (seafloor) diagenetic magnetite
115 (e.g., Zegeye et al. 2012; Bauer et al. 2020) is scarce. In this paper, we conducted a detailed

116 petrographic analysis on the BIF samples from the Neoarchean Baizhiyan Formation (North
117 China) supplemented with elemental geochemistry. These observations may help elucidate the
118 origins of BIFs, and will have significant implications for biogeochemical cycling in the
119 Neoarchean oceans (cf., Zegeye et al. 2012; Halevy et al. 2017; Rasmussen and Muhling 2018).
120

121 ## GEOLOGICAL SETTING

122 The studied area is located in the Neoarchean–Paleoproterozoic Trans-North China orogen,
123 along which the Eastern Archean Block and Western Paleoproterozoic Block were amalgamated
124 together to form the North China Craton at ca. 1.85 Ga (Fig. 1a; Zhao et al. 2005; Li et al. 2010).
125 The middle segment of the Trans-North China orogen is represented by the Hengshan-Wutai-
126 Fuping Belt (also known as the Wutai complex; Fig. 1b). Within this orogenic belt, the Wutai
127 complex is characterized by greenschist- to lower amphibolite-facies in the middle part and is
128 regarded as a typical granite-greenstone belt, while the Fuping and Hengshan complexes that are
129 dominated by amphibolite to granulite facies are located in the southeast and northwest parts of
130 the belt, respectively (Bai 1986; Tian 1991; Bai et al. 1992). The Wutai complex, commonly
131 referred to the Wutai Group in Chinese literature (cf. Han et al. 2017), is composed of
132 Neoarchean to Paleoproterozoic granitoids and metamorphosed volcanic and sedimentary rocks.
133 This group has been subdivided into three lithotectonic units: the Shizui, Taihuai and Gaofan
134 subgroups (Fig. 2; Han et al. 2017). These three imbricated lithotectonic units were structurally
135 disrupted and juxtaposed along a series of NE-SW-trending ductile shear zones (Han et al. 2017).
136 The studied Baizhiyan Formation, together with the overlying Hongmenyan Formation,
137 constitute the Taihuai subgroup. This subgroup consists of felsic volcanic rocks and tholeiites of
138 volcanic-arc affinity, intruded by calc-alkaline granitoid plutons that have been metamorphosed

139 to greenschist facies, and is interpreted as a Neoarchean-Paleoproterozoic accretionary arc (Bai
140 and Dai 1998; Wu and Zhong 1998; Wang et al. 2004). The BIF in the Taihuai subgroup is well-
141 developed and intimately associated with felsic and mafic volcanic rocks (Wang et al. 2004; Han
142 et al. 2017; Men et al. 2020), and has been interpreted as Algoma-type BIF based upon its
143 volcano-sedimentary lithofacies associations (e.g., Han et al. 2017; Men et al. 2020).

144 The age of the Wutai Group is well constrained based on a series of zircon U-Pb ages
145 (compiled in Han et al. 2017). The Shizui, Taihuai and Gaofan subgroups are likely deposited at
146 ca. 2.54–2.51 Ga, ca. 2.51–2.53 Ga and ca. 2.53 Ga, respectively (cf. Wilde et al. 2004, 2005;
147 Wang et al. 2014; Han et al. 2017; Fig. 2). It should be noted that the terms ‘‘Formation”,
148 “Subgroup” and ‘‘Group” applied to these units are the results of historical precedence, rather
149 than in the sense of formal stratigraphic units, because the original stratigraphic sequences are
150 not clearly preserved due to intense structural deformation (cf., Han et al. 2017). The
151 geochronological constraints of the different subgroups within the Wutai Group often overlap,
152 indicating that they are at least partially correlative. The Baizhiyan Formation is dated directly
153 using sensitive high-resolution ion microprobe zircon U-Pb geochronology on samples from the
154 felsic tuff in Ekou iron mine (Fig. 1c), giving an age of 2524 ± 10 Ma (Wilde et al. 2004). Thus,
155 BIFs in the Baizhiyan Formation were likely deposited at ca. 2.52 Ga, on the eve of the transition
156 to a persistently oxidizing atmosphere known as the Great Oxidation Event (GOE; onset
157 constrained to ca. 2.50–2.43 Ga by Warke et al. 2020).

158 The BIFs of the Baizhiyan Formation are composed of alternating iron-rich and silica-rich
159 bands, and lack significant detrital components (Fig. 3). Some siderite-rich layers within iron-
160 rich bands are present (Fig. 3e and f), commonly ~0.2 mm in thickness, and feature matrix-
161 supported, angular quartz grains (Fig. 3f). These bands are generally centimeter-scale in

thickness, and are undeformed or mildly folded (Fig. 3). No unequivocal primary wave/current structures were identified, although some may have been locally obscured by deformation. Rare bands feature intraclast breccias, while the adjacent bands are comparatively undeformed (Fig. 3c). This *in situ* brecciation may suggest reworking of chert hardgrounds by storm current activity (e.g., Trower and Lowe 2016), though synsedimentary tectonism may have played a role (Rasmussen et al. 2015a). We interpret the BIFs of the Baizhiyan Formation to have been largely deposited in an environment below storm wave base and distal from terrestrial siliciclastic inputs.

SAMPLES AND METHODS

Samples analyzed in this study were collected from an iron mine at the Yangjiaogou Village (38°59′09.16″N, 113°14′02.21″E), Dai County (northern Shanxi, North China, Fig. 1). The surfaces of samples were removed using a lapidary rock saw, and only the central, best-preserved parts were reserved. These samples were subsequently cut and separated into iron-rich and silica-rich bands for mineralogical and geochemical analyses. For geochemical analyses, fresh chips were cleaned, dried, and then ground into fine powders (~200 mesh) in an agate mortar avoiding any metal contact.

In order to produce smooth sample surfaces for electron microscopy, ion milling was conducted in the field emission scanning electron microscope (FESEM) Laboratory, China University of Geosciences (Beijing) with Gatan Ilion 697 ion mills. Sample surfaces were mechanically polished using successively finer grit (down to 1 μm grit size) and were then milled for two hours at 6 kV and a beam incident angle of 60°. This approach produced smooth surfaces for latter examination by FESEM, energy disperse spectroscopy (EDS) and electron backscatter diffraction (EBSD).

Petrographic analysis was conducted on argon ion milling chips using a Zeiss Supra 55 FESEM under 20 kV accelerating voltage with a working distance of ~15 mm, in the FESEM Laboratory, China University of Geosciences (Beijing). A secondary electron imaging detector was used to characterize topographic features, and an AsB detector was used to reveal compositional difference (backscattered electron image; BSE). Samples were coated with ~4 nm thick carbon before analysis.

Elemental concentrations of micron-sized spots were quantitatively analyzed by an Oxford EDS connected to the FESEM, operated at 20 kV with a working distance of ~15 mm and beam diameter of ~2 μm, in the FESEM Laboratory, China University of Geosciences (Beijing). Minerals and synthetic phases (MINM25-53) were used as reference standards. Duplicate analyses of individual points showed analytical error less than 3%.

EBSD measurements were carried out in the FESEM Laboratory using a Zeiss SUPRA 55 FESEM with an Oxford NordlysNano EBSD acquisition camera. The measurements were collected using an accelerating voltage of 20 kV, 200 nA beam current, and a working distance of ~25 mm. The sample surface was tilted 70° relative to horizontal to enlarge the beam-specimen activation so that the EBSD signal can be enhanced. Diffraction patterns were manually collected, and automatically indexed in real-time using the AZtec software from the HKL Technology, Oxford Instruments. Six to eight Kikuchi bands were included for the fitting algorithm. Only measurements with mean angular deviation (MAD) values below 1.0° were accepted for analyses, and the indexing rate is about 80%.

Eighteen bulk rock powder samples (from 9 iron-rich bands and 9 silica-rich bands) were chosen for X-ray diffraction (XRD) analysis. The samples were scanned after air-drying. The powder slides were scanned from 4° to 70° with a step size of 0.02° 2θ and a scan speed of

208 1°/min, using nickel filter copper radiation in a SmartLab X-Ray Diffractometer at China
209 University of Geosciences (Beijing).

210 For major element analyses of BIF bands, about 50 mg sample powder was dissolved in 250
211 mg lithium metaborate at 990 °C for 20 mins and then diluted to 100 ml by MQ before element
212 measurement using inductively coupled plasma optical emission spectrometry (ICP-OES) at
213 China University of Geosciences (Beijing). The accuracy for all ICP-OES analyses is better than
214 5% (relative) for analyzed elements.

215 The procedure for trace element analysis of the BIFs was modified from Zhou et al. (2018).
216 About 25 mg of fine powder for each sample was weighed out and dissolved using 1.5 mL HF
217 and 0.5 mL HNO_3 in a Teflon bomb, and heated at 220 °C for 24 h. After evaporating sample
218 solution to dryness on 170 °C hot plate, 0.5 mL HNO_3 was added, and repeated four times. After
219 adding 2.5 mL of HNO_3, the Teflon bomb was sealed and heated at 150 °C for 4 h. After cooling,
220 the solution was transferred to a plastic bottle, and diluted with ultrapure water to 25 mL. The
221 trace elements were measured by PerkinElmer NexION 300Q inductively coupled plasma mass
222 spectrometry (ICP-MS) at the National Research Center for Geoanalysis, Beijing. The accuracy
223 for all ICP-MS analyses is better than 5−10% (relative) for analyzed elements.

224

225 **RESULTS**

226 The petrographic and geochemical results are shown in Figs. 4−6, and Tables S1 and S2.
227 Iron-rich bands of the Baizhiyan Formation BIFs (69 ± 16 wt% (1SD) TFe_2O_3; 18 ± 17 wt%
228 (1SD) SiO_2; n = 9) are mainly composed of magnetite, with minor quartz, siderite and ankerite;
229 while the silica-rich bands (15 ± 1.6 wt% TFe_2O_3; 71 ± 11 wt% SiO_2; n = 9) are largely
230 composed of quartz, with minor amount of magnetite, siderite and chamosite. Fine (sub-mm-

231 scale) laminae of siderite are also documented within iron-rich bands (Fig. 3e and f).
232 Petrographic analysis indicates that detrital siliciclastic grains are exceedingly rare within the
233 BIFs, which is in good accordance with the low Al_2O_3 content (0.7 ± 0.7 wt% for iron-rich bands,
234 and 0.3 ± 0.6 wt% for silica-rich bands). P_2O_5 contents in the Baizhiyan BIFs range from 0.05
235 wt% to 0.51 wt%, showing good correlation with TFe_2O_3 contents (R^2 = 0.74; Fig. 6).

236 In order to further understand the origin and significance of the BIF magnetite, we focused
237 on the magnetite particles within the silica-rich bands (Fig. 4). Chert bands in BIFs can afford
238 exceptional preservation of other authigenic phases due to early silicification at the sediment–
239 seawater interface (e.g., Rasmussen et al., 2019). The mineralogy of magnetite is determined
240 using multiple methods, including quantitative EDS (Fig. 4d), EBSD (Fig. 4e) and XRD (Fig. 5)
241 analyses. These magnetite crystals are anhedral to euhedral in morphology and 3–30 μm in size,
242 and euhedral magnetite can feature a hexagonal habit (Fig. 4b, c, f–h). The hexagonal magnetite
243 crystals are present as thin flakes and are mainly surrounded by quartz cement, though some are
244 in close contact with anhedral siderite (Fig. 4). As discussed further below, these hexagonal
245 magnetite crystals are morphologically similar to hexagonal platelets of green rust identified in
246 laboratory experiment (e.g., Li et al. 2017).

247 The trace element geochemistry of the Baizhiyan BIFs can offer further insights into their
248 genesis. The REE+Y patterns of iron-rich and silica-rich bands show similar features (Fig. 7).
249 These include prominently positive Eu anomalies (Eu_{SN}/Eu_{SN}^* < 3.9), a depletion of light REEs
250 (Pr_{SN}/Yb_{SN} = 0.30 ± 0.14), and no to slightly positive Ce anomalies (Ce_{SN}/Ce_{SN}^* = 0.97 ± 0.07;
251 Fig. 8 and Table S3). The Y/Ho ratio ranges from 24.9 to 44.6 (Table S3). There is no correlation
252 between Th and total REE content (ΣREE), Y/Ho, Pr_{SN}/Yb_{SN}, Ce_{SN}/Ce_{SN}^* or Eu_{SN}/Eu_{SN}^* (Fig. 8),
253 and no correlation exists between ΣREE and Ce_{SN}/Ce_{SN}^* (Fig. 8).

This is the peer-reviewed, final accepted version for American Mineralogist, published by the Mineralogical Society of America.
The published version is subject to change. Cite as Authors (Year) Title. American Mineralogist, in press.
DOI: https://doi.org/10.2138/am-2022-7981. http://www.minsocam.org/

DISCUSSION

Seawater redox background

Iron formations are relatively pure (bio)chemical sediments and typically feature minor amount of detrital contamination (Konhauser et al. 2017), and are commonly taken as reliable archives of geochemical indices of seawater chemistry (e.g., Planavsky et al. 2010; Robbins et al. 2016). In our samples, the contents of the geochemical proxies for detrital contamination are low, such as Al (0.25 ± 0.36 wt%) and Zr, Th, Hf and Sc (all < 20 μg/g) (Tables S2 and S3). The lack of correlation between detrital proxies (e.g., Th) and ΣREE or other REE signatures (e.g., Y/Ho, Pr_{SN}/Yb_{SN}, Ce_{SN}/Ce_{SN}* and Eu_{SN}/Eu_{SN}*) (Fig. 8) suggests that the REE composition of the BIFs has experienced negligible detrital contamination. In modern oceans, shallow seawater features a characteristic REE signature that results from the differential scavenging of REEs according to their relative stability in seawater. This results in a light REE depleted pattern, with strongly positive La anomaly, negative Ce anomaly, slightly positive Gd anomaly, and high Y/Ho ratio (> 36), which are often taken as indicative of seawater REE patterns in sedimentary rocks (e.g., Webb and Kamber 2000; Ling et al. 2013; Tang et al. 2016). The REE characteristics of seawater are likely to have varied throughout geological time, particularly with respect to the redox-sensitive Ce and Eu (e.g., Fryer 1977; Derry and Jacobsen 1990). However, a strong Y enrichment is often considered diagnostic of seawater REE profiles and more muted Y enrichments may reflect detrital siliciclastic contamination (e.g., Bau and Dulski 1996; Webb and Kamber 2000). Therefore, although petrographic and geochemical evidence suggests that the siliciclastic influence on the Baizhiyan BIFs is negligible, we filter our results to exclude samples with $Pr_{SN}/Yb_{SN} > 0.5$ and Y/Ho < 32 from further analysis in order to interpret those

277 samples considered to represent the purest seawater signals.

278 Following geochemical screening, several samples of the Baizhiyan BIFs feature REE
279 patterns that share some similarities with modern seawater, including a general light REE
280 depletion (average Pr_{SN}/Yb_{SN} = 0.23; n = 8) and Y enrichment (average Y/Ho = 36.3; n = 8),
281 which may support the interpretation that these represent marine signatures. However, the most
282 prominent difference in the REE patterns between the Baizhiyan BIFs and modern shallow
283 seawater is that the REE of Baizhiyan BIFs either lack Ce anomalies (i.e., $0.95 < Ce_{SN}/Ce_{SN}^* <$
284 1.05), or feature slightly positive Ce anomalies ($Ce_{SN}/Ce_{SN}^* \geq 1.05$) in both filtered (average
285 Ce_{SN}/Ce_{SN}^* = 1.05; n = 8) or unfiltered (average Ce_{SN}/Ce_{SN}^* = 1.03; n = 18) samples. Cerium
286 anomalies are related to environmental redox conditions, because Ce is unique among the REEs
287 in that has trivalent and tetravalent oxidation states (de Baar et al. 1988; German and Elderfield
288 1989; Sholkovitz and Schneider 1991). In modern oxygenated seawater, Ce(III) is rapidly
289 oxidized to Ce(IV) coupled with Fe and Mn redox cycling, and is efficiently scavenged by
290 precipitating Fe-Mn-hydroxides and organic complexes, resulting in negative Ce anomalies in
291 the water column (Byrne and Sholkovitz 1996). In contrast, in the predominantly anoxic water
292 columns such as those that were characteristic of the Archean and Paleoproterozoic oceans,
293 reductive dissolution maintains Ce in the seawater column and results in negligible or positive
294 Ce anomalies (e.g., Planavsky et al. 2010). The lack of significant negative Ce anomalies in the
295 Baizhiyan BIFs, therefore, likely indicates that at least the bottom waters of the depositional
296 basin were anoxic (e.g., Planavsky et al. 2010; Liu et al. 2019).

297 The thin siderite laminae interbedded with the magnetitic BIF horizons may suggest that the
298 siderite was syndepositional and accumulated at or near the sediment–seawater interface (Xie et
299 al. 2021). The precipitation of siderite requires anoxic and ferruginous fluid conditions with high

alkalinity and low sulfate concentrations (e.g., Berner 1981; Mozley 1989; Romanek et al. 2009). In well-oxygenated marine environments, such as those characteristics of the Phanerozoic, siderite authigenesis is restricted to ferruginous porewater (e.g., Berner 1971; Armenteros, 2010). However, for the dominantly ferruginous Precambrian oceans (e.g., Reinhard et al. 2013; Planavsky et al. 2014a), it is conceivable that requisite conditions for the precipitation of siderite (including Fe(II) and bicarbonate concentrations) could be met in the water column (e.g. Beukes et al. 1990; Tice and Lowe 2004). Indeed, siderite is a common constituent of many Archean–Paleoproterozoic IFs (e.g., Klein 2005). There is strong isotopic evidence that siderite in IFs has formed via dissimilatory iron reduction during early diagenesis (Konhauser et al. 2005; Johnson et al. 2003; 2008a; Heimann et al. 2010; Posth et al. 2013b; Tang et al. 2018). Alternatively, some Precambrian siderite deposits may have formed via primary precipitation at a seawater redoxcline (Beukes and Klein 1990; Tice and Lowe 2004). The seawater-like carbon isotope composition of siderite in many BIFs has been used to argue for a seawater source for the requisite bicarbonate (Ohmoto et al. 2004; Pecoits et al. 2009; Wittkop et al. 2014; Garcia et al. 2016). A marine origin for bicarbonate may support models in which siderite is transformed from green rust as has been shown to occur experimentally (Halevy et al. 2017). However, the observation of siderite intraclasts within IFs (e.g., Beukes et al. 1990) suggests that regardless of whether the siderite is primary or early diagenetic, in many cases siderite genesis is essentially syndepositional. The siderite layers of the Baizhiyan BIFs are sub-millimeter in thickness, and no deformation caused by the displacive growth of siderite layers has been identified in the adjacent layers (Fig. 3e and f), arguing against the diagenetic displacive growth of the siderite layers (cf., Liu et al. 2019). In addition, siderite occurs as matrix supporting isolated quartz and feldspar sand clasts, likely suggesting that the siderite accumulated as background deposition from the

323 water column or at the seafloor contemporaneous with the supply of sand grains. The close
324 association of the hexagonal magnetite with siderite crystals in chert bands (Fig. 4b) is similar to
325 the mineralogical associations of Holocene sediments deposited in the ferruginous Lake Towuti
326 (Indonesia), where primary green rust and magnetite accumulate at the sediment–seawater
327 interface, and closely associated siderite forms via the diagenetic reduction of Fe-Mn phases
328 coupled with organic matter degradation (Vuillemin et al. 2019). Dissimilatory iron reduction has
329 been suggested to have been particularly active during the Neoarchean due to a high flux of
330 ferric (oxyhydr)oxides and organic matter from the photic zone coupled with low seawater
331 sulfate (Johnson et al., 2008b). Overall, the mineralogy and geochemistry of the Baizhiyan BIFs
332 is consistent with a model wherein iron cycling in a predominantly anoxic water column results
333 in the accumulation of early diagenetic magnetite, siderite and silica at the sediment–seawater
334 interface.
335
336 **Iron source**
337 The source of iron for IF genesis is an issue of ongoing debate. Three major viewpoints
338 have been suggested for the iron source: 1) the redox cycling of continentally sourced weathering
339 inputs (e.g., Dymek and Klein 1988; Bau and Möller 1993), 2) a marine Fe(II) reservoir
340 dominantly supplied by hydrothermal fluids (e.g., Bekker et al. 2010; Rasmussen et al. 2012),
341 and 3) a combination of the two (e.g., Alexander et al. 2008; Li et al. 2015). Since positive Eu
342 anomaly in hydrothermal fluid is linked to the breakdown of plagioclase in volcanic rocks
343 underlying hydrothermal vents at relatively high temperatures (> 250 °C) (Schnetzler and
344 Philpotts 1970; Graf 1977, 1978; Fryer et al. 1979), positive Eu anomalies in chemical
345 sedimentary rocks precipitated from seawater have been widely used as an indicator of the

346 influence of high-temperature hydrothermal fluids (e.g., Klinkhammer et al. 1983; Derry and
347 Jacobsen 1988, 1990; Bau and Dulski 1996; Viehmann et al. 2015). Therefore, although
348 deposition may have taken place in a water column characterized by a flux of Fe(II) sourced
349 from benthic Fe(III) reduction (e.g., Li et al. 2015), the prominent positive Eu anomalies in the
350 Baizhiyan BIFs (Eu_{SN}/Eu_{SN}* up to 3.9) probably reflects a contribution from locally sourced,
351 high temperature hydrothermal fluids (Halverson et al. 2011; Raye et al. 2015; Wang et al. 2016;
352 Sylvestre et al. 2017). This explanation is consistent with the accretionary arc geological setting
353 suggested previously for this formation and also in agreement with the observation that the BIFs
354 are intimately associated with felsic and mafic volcanic rocks in this formation (Wang et al. 2004;
355 Han et al. 2017; Men et al. 2020).
356
357 **Genesis of magnetite**
358 The origin of magnetite in IFs remains debated. There is abundant petrographic evidence
359 that in many (or most) cases, magnetite is demonstrably secondary and replacing or overprinting
360 earlier phases such as hematite or siderite (e.g., Han 1978; Ewers and Morris 1981; Kaufman
361 1996; Krapež et al. 2003; Beukes and Gutzmer 2008). The metamorphic reduction of ferric
362 oxides such as hematite can lead to replacement by magnetite (Mücke and Cabral 2005).
363 Laboratory experiments also show that magnetite can form via the thermal decomposition of
364 siderite (Gallagher and Warne 1981) or the transformation of ferrihydrite and glucose through
365 thermal decarboxylation processes (Posth et al. 2013b; Köhler et al. 2013).
366 However, evidence from laboratory-based experiments suggest that primary or early
367 diagenetic magnetite could have played a role during IF genesis. Magnetite (and/or precursor
368 green rust phases) can be synthesized via the (partial) oxidation of Fe(II) (Stumm and Lee 1961;

Génin et al. 2006; Halevy et al. 2017) or the interaction of aqueous Fe(II) and ferric (oxyhydr)oxides (Ruby et al. 2006; Usman et al. 2012a, 2012b). Microbial activity may be important. Anaerobic Fe(II) oxidation by nitrate-reducing bacteria has been shown to lead to the generation of hexagonal platelets of green rust (Chaudhuri et al. 2001; Pantke et al. 2012) and the subsequent transformation to magnetite (Miot et al. 2014), and phototrophic Fe(II)-oxidizing bacteria can also facilitate magnetite formation (Jiao et al. 2005).

The bacterial reduction of ferric oxyhydroxides (such as ferrihydrite) is also an important process in the generation of magnetite, with or without a green rust precursor phase (e.g., Fredrickson et al. 1998; Ona-Nguema et al. 2002; Zegeye et al. 2010; Li 2012). The product is dependent upon several factors including reduction rates, bacterial cell density, pH, temperature or the availability of anions (Zegeye et al. 2010; O'Loughlin et al. 2015; Usman et al. 2018). Passible evidence for an early diagenetic (i.e., dissimilatory iron reduction) origin of magnetite in IFs includes iron isotope data, whereby the negative iron isotope (δ^{56}Fe) values of many magnetite-bearing IFs are comparable to the negative fractionations measured in experimental culture with iron reducing bacteria (e.g., Johnson et al. 2008a; Li et al. 2013b). Further, some IF magnetite features a unique crystallography (i.e., lattice constant and Fe^{2+}/Fe^{3+} stoichiometry) similar to biologically generated extracellular magnetite generated by dissimilatory iron reducing bacteria (Li et al. 2011).

Magnetite has also been shown to be a syndepositional phase in sediments deposited in modern ferruginous lakes (Zegeye et al. 2012; Vuillemin et al. 2019; Bauer et al. 2020). In these settings, settling ferrihydrite formed in surface waters can be microbially reduced to form globular magnetite (Bauer et al. 2020). Alternatively, ferrihydrite in ferruginous lakes has also been shown to react with water column Fe(II) and form metastable green rust, which rapidly

transforms to magnetite in the water column (Zegeye et al. 2012). This primary transformation of magnetite from green rust under ferruginous conditions is supported by thermodynamic modelling and experimental observations (Halevy et al. 2017; Li et al. 2017). Magnetite and/or green rust formed in the water column may potentially be able to directly archive seawater chemistry.

In redox stratified seawater (such as is envisaged for much of the Precambrian; Lyons et al. 2014), the oxidation of Fe(II) could have taken place above the redoxcline (by molecular oxygen generated by oxygenic photosynthesizers, either via direct reaction or facilitated by chemotrophic iron oxidizing bacteria). Alternatively, Fe(II) oxidation could have been facilitated below the redoxcline by anoxygenic photosynthesizers as has been documented in the ferruginous Lake Matano (Indonesia; Crowe et al. 2008), and is interpreted for other Neoarchean BIFs (e.g., Rego et al. 2021). These processes could have produced primary ferrihydrite, and during the settling of ferrihydrite in anoxic seawater or on the seafloor, some of this ferrihydrite could also have been transformed into green rust (Zegeye et al. 2012; Li et al. 2017), possibly involving dissimilatory iron reduction. In laboratory experiments, the rapid formation of green rust is observed when ambient temperature is greater than 50 °C (Li et al. 2017), but in the Lake Matano, green rust is formed at lower temperatures (Zegeye et al. 2012). Under anoxic conditions and with proper Fe(II):Fe(III) ratio, metastable green rust can transform to magnetite (Li et al. 2017; Halevy et al. 2017).

Evidence from magnetite morphology

Green rust commonly forms as hexagonal flakes with sizes of submicron to several microns (Wiesli et al. 2004; Sumoondur et al. 2008; Zegeye et al. 2012; Halevy et al. 2017; Li et al. 2017;

Usman et al. 2018), and the magnetite transformed from metastable green rust has the potential to inherit the hexagonal morphology and to form green rust pseudomorphs. During the experimental generation of magnetite via a green rust precursor, the magnetite formed is typically either isometric (e.g., Sumoondur et al. 2008) or aggregates of nanoparticles (Li et al. 2017). However, these experiments indicate that the transformation of green rust to magnetite takes place via dissolution and reprecipitation or *in situ* deprotonation (Sumoondur et al. 2008; Ruby et al. 2010; Li et al. 2017). Therefore, we propose that rapid silicification on the seafloor may have aided in the preservation of green rust morphology during transformation to magnetite. Thus, the presence of hexagonal flakes of magnetite in IFs may be a significant indicator for its green rust precursor. The conditions required to facilitate green rust formation and transformation into magnetite (i.e., anoxic and ferruginous conditions; Sumoondur et al. 2008; Zegeye et al. 2012; Halevy et al. 2017; Li et al. 2017) would have been present in the hydrothermally influenced depositional setting envisaged for many Algoma-type BIFs, which may therefore preserve evidence of green rust iron cycling in deep time.

In the studied samples, hexagonal magnetite is preserved in the Baizhiyan BIFs (Fig. 4). This is a unique habit that is distinct from euhedral magnetite formed from other processes, which most commonly shows octahedral and dodecahedral forms (Matthews 1976; Heider et al. 1987). The biomineralization of intracellular magnetite by magnetotactic bacteria (i.e., magnetosomal magnetite) can be hexagonal, but is typically elongated along the [111] axis (e.g., Meldrum et al. 1993; Li et al. 2020), rather than equant like the hexagonal platelets of green rust and the magnetite of this study (Fig. 4). However, small (<50 nm) hexagonal magnetite platelets have been documented forming from reaction of ferric (oxyhydr)oxides with Fe(II) (Usman et al. 2012a). Dissimilatory iron reduction by thermophilic bacteria can form large hexagonal

438 magnetite platelets (<350 nm) at elevated temperatures (65 °C) and long incubation times
439 (several years; Li 2012). It is unclear whether green rust may have played an intermediary role in
440 these processes. However, hexagonal morphology is much more common to green rust than
441 magnetite, and although magnetite may be thermodynamically more stable, the formation of a
442 green rust precursor may be kinetically favored (Usman et al. 2012b; Halevy et al. 2017).

443 The Baizhiyan hexagonal magnetite is sometimes in contact with siderite (Fig. 4c), likely
444 suggesting that they were precipitated contemporaneously and transformed from green rust for
445 reasons of redox balance (Halevy et al. 2017). Magnetite transformed from siderite during
446 metamorphism ($3FeCO_3 + H_2O \rightarrow Fe_3O_4 + 3CO_2 + H_2$) (Rasmussen and Muhling 2018) typically
447 forms elongated simple octahedron (or cubo-octahedron) or, less commonly, truncated hexa-
448 octahedron (Golden et al. 2004) rather than hexagonal platelets. The biological oxidation of
449 siderite by nitrate-reducing bacteria can also produce magnetite (Chaudhuri et al. 2001).
450 However, despite the local association, most magnetite crystals documented from Baizhiyan
451 BIFs are dispersed in chert and not associated with siderite, suggesting that the transformation of
452 siderite is likely not responsible for the hexagonal magnetite (cf., Rasmussen and Muhling 2018).
453 There are no relics of iron silicates closely associated with hexagonal magnetite. The positive
454 correlation between Fe and P (Fig. 6) further indicates that the precursors of these magnetites are
455 more likely Fe-hydroxides or green rust rather than greenalite, since both Fe-hydroxides and
456 green rusts strongly adsorb P (Zegeye et al. 2012).

457 Hematite, transformed from Fe-hydroxides, can also form a hexagonal platelet habit, as
458 demonstrated from experimental, hydrothermal synthesis (Peng et al. 2010) and microbial
459 biofilms (Sawicki et al. 1995). Rare hexagonal platelets of hematite have been described from
460 modern lateritic soils (Schwertmann and Kämpf 1985), in ancient marine red beds (Eren and

461 Kadir 1999; Tang et al. 2020) and in BIFs (Han 1982; Lantink et al. 2018). However, it is
462 unlikely that the hexagonal magnetite represents a pseudomorph after hematite platelets. The
463 reaction between hematite and Fe(II)-bearing fluids during metamorphism could lead to the
464 formation of magnetite (Pedersen et al. 2005). This process, however, tends to either form
465 euhedral magnetite crystals (typically octahedra or truncated octahedra) that are much larger than
466 the precursor hematite or porphyroblasts that are intergrown and texturally destructive (Han 1982;
467 Otake et al. 2007). Further, the large-scale replacement of a hematite-dominated BIF by
468 magnetite may require unreasonably large volume of metamorphic fluids to alter the massive
469 amount of iron oxides in BIFs (Morris 1985). In our study, hexagonal magnetite crystals are
470 generally away from veins, and in impermeable silica-rich bands (Fig. 4). Therefore, we suggest
471 that they are not likely to have transformed from hematite.

472 We suggest that the hexagonal magnetite platelets of the Baizhiyan BIFs were most likely
473 transformed from green rust during deposition and early (i.e., seafloor) diagenesis at or near the
474 sediment–seafloor interface (cf., Li et al. 2017). The anoxic and ferruginous bottom seawater
475 conditions (as indicated by the lack of negative Ce anomalies; Fig. 8) in the studied interval
476 would have facilitated the formation of green rust and its subsequent transformation into
477 magnetite (Fig. 9). This formation of green rust could have been enhanced or facilitated by
478 dissimilatory iron reduction. The size of green rust hexagonal platelets observed in modern
479 ferruginous lakes and experiments are commonly less than 5 μm, consistent with some of the
480 hexagonal platelets observed in our study (Fig. 4f–g). However, some of the hexagonal magnetite
481 crystals of the Baizhiyan BIFs are larger than 5 μm (< 50 μm; Fig. 4h). During experimental
482 synthesis of green rust, longer aging tends to lead to larger hexagonal platelets (Barthélémy et al.
483 2012; Géhin et al. 2002). Interestingly, the large, hexagonal platelets of the biologically mediated

484 magnetite produced experimentally by Li (2012) were produced using a long incubation time (<7
485 years). Evidence from modern ferruginous lakes suggests that under anoxic conditions green rust
486 may be stable on early diagenetic timescales prior to its transformation to magnetite (Vuillemin
487 et al. 2019). The large crystal size of the hexagonal magnetite of the Baizhiyan BIF may be the
488 product of prolonged aging of green rust under early diagenetic conditions. The presence of
489 organic matter during deposition may have also stabilized the mixed-valence phases (O'Loughlin
490 et al. 2010). Another plausible explanation could be that the large sized hexagonal magnetite
491 resulted from further overgrowth or from the aggregation of several original green rust particles,
492 from more favorable growth conditions such as higher Fe(II) concentration and/or higher
493 temperature in Neoarchean seawater. Further experimental work is required to elucidate the
494 genesis of these larger platelets.

495 **IMPLICATIONS**

496 Unravelling the complex paragenesis of IFs and identifying the primary mineralogy are
497 essential for extracting paleoenvironmental information from IFs. Since green rust is a ferrous-
498 ferric hydroxy salt, its formation requires a redox cycling of iron in the water column. In contrast,
499 the interpretation of greenalite as a precursor phase for the iron oxides of IFs would imply its
500 formation under anoxic and ferruginous seawater conditions without iron redox cycling
501 (Rasmussen et al. 2013, 2015a, 2015b, 2017; Tosca et al. 2016). However, several lines of
502 evidence point to active role of redox cycling in the lead-up to the GOE (ca. 2.5–2.3 Ga; e.g.,
503 Lyons et al. 2014), including iron isotope fractionations preserved in the ferric oxides of IFs (e.g.,
504 Dauphas et al. 2017). As such, iron oxide-bearing IFs are more commonly interpreted to form
505 from primary Fe(III) oxyhydroxides (ferrihydrite) or Fe(III)-Si gels (e.g., Konhauser et al. 2017).
506 In this study, we suggest that the hexagonal magnetite crystals preserved within chert bands

present evidence that at least some of the magnetites in the Baizhiyan BIFs represent the product of primary green rust formed in the Neoarchean water column (cf., Zegeye et al. 2012; Halevy et al. 2017; Li et al. 2017). Anoxic bottom waters would have facilitated the transformation of this green rust to magnetite rather than more oxidized species such as ferrihydrite (Ruby et al. 2010). Regardless of the specific genetic pathway, the interpretation of the formation of primary mixed-valence iron phases supports the hypothesis that marine iron redox cycling played a key role in IF genesis before the GOE (Fig. 9). In this case, the Fe(III) required for green rust formation could have resulted from oxidation either by molecular oxygen generated by cyanobacteria (possibly mediated by chemotrophic iron oxidizing bacteria) or by anoxygenic photosynthetic iron oxidizing bacteria (Fig. 9; cf., Halevy et al. 2017; Li et al. 2017; Lin et al. 2019). Therefore, our results support models in which the formation of a combination of different primary minerals—including ferric phases (such as ferrihydrite), ferrous phases (such as greenalite), and mixed valence phases (such as green rust/magnetite)—were important processes to be considered in BIF genesis (e.g., Halevy et al. 2017; Konhauser et al. 2017; Koeksoy et al. 2019).

Oxygenic photosynthesis is suggested to have been active for hundreds of millions of years prior to the oxygenation of the atmosphere (Anbar et al. 2007; Planavsky et al. 2014b; Koehler et al. 2018). In order to maintain a low oxygen atmosphere–ocean system, low primary productivity is likely required during this time, which may be a consequence of nutrient limitation (e.g., Laakso and Schrag 2018). Green rust has a much stronger ability of adsorbing nutrients such as P and Ni than ferrihydrite (Hansen and Poulsen 1999; Zegeye et al. 2012). Therefore, it may have exerted a great influence on Precambrian biogeochemical cycles (Zegeye et al. 2012; Halevy et al. 2017; Koeksoy et al. 2019). If green rust precipitation was an important process in Neoarchean shallow seawaters globally, bioavailable phosphorus would be efficiently scavenged,

resulting in oligotrophic conditions, and hence low primary production. This would in turn lead to low organic carbon burial and oxygen production (cf., Guilbaud et al. 2020). Therefore, generation of green rust in Precambrian shallow seawaters may have been one of the causes leading to a protracted oxygenation of Earth surface system.

ACKNOWLEDGMENTS

The study was supported by the National Natural Science Foundation of China (Nos. 41930320, 41972028), the Key Research Program of the Institute of Geology & Geophysics, CAS (No. IGGCAS-201905), the Chinese "111" project (B20011), and by the Fundamental Research Funds for the Central Universities (Nos. 2652019093, 2652019250). Maxwell Lechte acknowledges a funding from the Fonds de Recherche du Québec—Nature et Technologies.

REFERENCES CITED

Alexander, B.W., Bau, M., Andersson, P., and Dulski, P. (2008) Continentally-derived solutes in shallow Archean seawater: rare earth element and Nd isotope evidence in iron formation from the 2.9 Ga Pongola Supergroup, South Africa. Geochimica et Cosmochimica Acta, 72, 378–394.

Anbar, A.D., Duan, Y., Lyons, T.W., Arnold, G.L., Kendall, B., Creaser, R.A., Kaufman, A.J., Gordon, G.W., Scott, C., Garvin, J., and Buick, R. (2007) A whiff of oxygen before the great oxidation event? Science, 317, 1903–1906.

Armenteros, I. (2010) Chapter 2 diagenesis of carbonates in continental settings. Developments in Sedimentology, 62, 61–135.

Ayers, D.E. (1972) Genesis of iron-bearing minerals in banded iron formation mesobands in the

553 Dales Gorge Member, Hamersley Group, Western Australia. Economic Geology, 67, 1214–
554 1233.
555 Bai, J. (1986) The Early Precambrian Geology of Wutaishan, 435 p. Tianjin Science and
556 Technology Press, Tianjin, China, (in Chinese).
557 Bai, J., and Dai, F.Y. (1998) Archean crust of China. Precambrian Crust Evolution of China, 86 p.
558 Geological Publishing House, Beijing, (in Chinese).
559 Bai, J., Wang, R.Z., and Guo, J.J. (1992) The Major Geologic Events of Early Precambrian and
560 Their Dating in Wutaishan Region, 55 p. Geological Publishing House, Beijing, (in
561 Chinese).
562 Barthélémy, K., Naille, S., Despas, C., Ruby, C., and Mallet, M. (2012) Carbonated ferric green
563 rust as a new material for efficient phosphate removal. Journal of Colloid and Interface
564 Science, 384, 121–127.
565 Bau, M., and Möller, P. (1993) Rare earth element systematics of the chemically precipitated
566 component in early Precambrian iron formations and the evolution of the terrestrial
567 atmosphere-hydrosphere-lithosphere system. Geochimica et Cosmochimica Acta, 57, 2239–
568 2249.
569 Bau, M., and Dulski, P. (1996) Distribution of yttrium and rare-earth elements in the Penge and
570 Kuruman iron-formations, Transvaal Supergroup, South Africa. Precambrian Research, 79,
571 37–55.
572 Bauer, K.W., Byrne, J.M., Kenward, P., Simister, R.L., and Crowe, S.A. (2020) Magnetite
573 biomineralization in ferruginous waters and early earth evolution. Earth and Planetary
574 Science Letters, 549, 116495.
575 Bekker, A., Slack, J.F., Planavsky, N., Krapež, B., Hofmann, A., Konhauser, K.O., and Rouxel,

O.J. (2010) Iron formation: the sedimentary product of a complex interplay among mantle, tectonic, oceanic, and biospheric processes. Economic Geology, 105, 467–508.

Bekker, A., Planavsky, N., Krapež, B., Rasmussen, B., Hofmann, A., Slack, J.F., Konhauser, K.O., and Rouxel, O.J. (2014) Iron Formations: Their Origins and Implications for Ancient Seawater Chemistry. Geochemistry, 12, 561–628.

Bell, P.E., Mills, A.L., and Herman, J.S. (1987) Biogeochemical conditions favoring magnetite formation during anaerobic iron reduction. Applied and Environmental Microbiology, 53, 2610–2616.

Berner, R.A. (1971) Principles of Chemical Sedimentology. American Journal of Science, 268, 1–13.

——— (1981) A new geochemical classification of sedimentary environments. Journal of Sedimentary Research, 51, 359–366.

Beukes, N.J., and Klein, C. (1990) Geochemistry and sedimentology of a facies transition—from microbanded to granular iron-formation—in the early Proterozoic Transvaal Supergroup, South Africa. Precambrian Research, 47, 99–139.

Beukes, N.J., and Gutzmer, J.E.N.S. (2008) Origin and paleoenvironmental significance of major iron formations at the Archean-Paleoproterozoic boundary. Economic Geology, 15, 5–47.

Beukes, N.J., Klein, C., Kaufman, A.J., and Hayes, J.M. (1990) Carbonate petrography, kerogen distribution, and carbon and oxygen isotope variations in an early Proterozoic transition from limestone to iron-formation deposition, Transvaal Supergroup, South Africa. Economic Geology, 85, 663–690.

Byrne R.H., and Sholkovitz E.R. (1996) Marine chemistry and geochemistry of the lanthanides. Handbook on the Physics and Chemistry of the Rare Earths, 23, 497–593.

599 Chaudhuri, S.K., Lack, J.G., and Coates, J.D. (2001) Biogenic Magnetite Formation through
600 Anaerobic Biooxidation of Fe(II). Applied and Environmental Microbiology, 67, 2844–
601 2848.
602 Cox, G.M., Halverson, G.P., Poirier, A., Le Heron, D., Strauss, J.V., and Stevenson, R. (2016) A
603 model for Cryogenian iron formation. Earth and Planetary Science Letters, 433, 280–292.
604 Crowe, S.A., Jones, C.A., Katsev, S., Magen, C., O'Neill, A.H., Sturm, A., Canfield, D.E.,
605 Haffner, G.D., Mucci, A., Sundby, B., Fowle, D.A. (2008) Photoferrotrophs thrive in an
606 Archean Ocean analogue. Proceedings of the National Academy of Sciences, 105, 15938–
607 15943.
608 Dauphas, N., John, S.G., and Rouxel, O. (2017) Iron isotope systematics. Reviews in Mineralogy
609 and Geochemistry, 82, 415–510.
610 de Baar, H.J., German, C.R., Elderfield, H., and Van Gaans, P. (1988) Rare earth element
611 distributions in anoxic waters of the Cariaco Trench. Geochimica et Cosmochimica Acta, 52,
612 1203–1219.
613 Derry, L.A., and Jacobsen, S.B. (1988) The Nd and Sr isotopic evolution of Proterozoic seawater.
614 Geophysical Research Letters, 15, 397–400.
615 ——— (1990) The chemical evolution of Precambrian seawater: evidence from REEs in banded
616 iron formations. Geochimica et Cosmochimica Acta, 54, 2965–2977.
617 Dymek, R.F., and Klein, C. (1988) Chemistry, petrology and origin of banded iron-formation
618 lithologies from the 3800 Ma isua supercrustal belt, West Greenland. Precambrian Research,
619 39, 247–302.
620 Eren, M., and Kadir, S. (1999) Colour origin of upper Cretaceous pelagic red sediments within
621 the Eastern Pontides, northeast Turkey. International Journal of Earth Sciences, 88, 593–595.

622 Eugster, H.P., and Chou, I.M. (1973) The depositional environments of Precambrian banded
623 iron-formations. Economic Geology, 68, 1144–1168.
624 Ewers, W.E., and Morris, R.C. (1981) Studies of the Dales Gorge Member of the Brockman Iron
625 Formation, Western Australia. Economic Geology, 76, 1929–1953.
626 Fischer, W.W., and Knoll, A.H. (2009) An iron shuttle for deepwater silica in Late Archean and
627 early Paleoproterozoic iron formation. Geological Society of America Bulletin, 121, 222–
628 235.
629 Fredrickson, J.K., Zachara, J.M., Kennedy, D.W., Dong, H., Onstott, T.C., Hinman, N.W., and Li,
630 S.M. (1998) Biogenic iron mineralization accompanying the dissimilatory reduction of
631 hydrous ferric oxide by a groundwater bacterium. Geochimica et Cosmochimica Acta, 62,
632 3239–3257.
633 Fryer, B.J. (1977) Rare earth evidence in iron-formations for changing Precambrian oxidation
634 states. Geochimica et Cosmochimica Acta, 41, 361–367.
635 Fryer, B.J., Kerrich, R., Hutchinson, R.W., Peirce, M.G., and Rogers, D.S. (1979) Archaean
636 precious-metal hydrothermal systems, Dome Mine, Abitibi Greenstone Belt. I. Patterns of
637 alteration and metal distribution. Canadian Journal of Earth Sciences, 16, 421–439.
638 Gallagher, P.K., and Warne, S. (1981) Thermomagnetometry and thermal decomposition of
639 siderite. Thermochimica Acta, 43, 253–267.
640 Garcia, T.I., Gorton, M.P., Li, H., Wortmann, U.G., and Spooner, E.T. (2016) The geochemistry
641 of the 2.75 Ga-old Helen Iron Formation, Wawa, Ontario–insights into iron formation
642 deposition from carbon isotopes and rare earth elements. Precambrian Research, 275, 357–
643 368.
644 Géhin, A., Ruby, C., Abdelmoula, M., Benali, O., Ghanbaja, J., Refait, P., and Génin, J.R. (2002)

Synthesis of Fe(II-III) hydroxysulphate green rust by coprecipitation. Solid State Sciences, 4, 61–66.

Génin, J.R., Ruby, C., Géhin, A., and Refait, P.C. (2006) Synthesis of green rusts by oxidation of $Fe(OH)_2$, their products of oxidation and reduction of ferric oxyhydroxides; Eh-pH Pourbaix diagrams. Comptes Rendus Geoscience, 338, 433–446.

German, C.R., and Elderfield, H. (1989) Rare earth elements in Saanich Inlet, British Columbia, a seasonally anoxic basin. Geochimica et Cosmochimica Acta, 53, 2561–2571.

Golden, D.C., Ming, D.W., Morris, R.V., Brearley, A.J., Lauer Jr, H.V., Treiman, A.H., Zolensky M.E., Schwandt, C.S., Lofgren, G.E., and McKay, G.A. (2004) Evidence for exclusively inorganic formation of magnetite in Martian meteorite ALH84001. American Mineralogist, 89, 681–695.

Graf, J.L. (1977) Rare earth elements as hydrothermal tracers during the formation of massive sulfide deposits in volcanic rocks. Economic Geology, 72, 527–548.

——— (1978) Rare earth elements, iron formations and sea water. Geochimica et Cosmochimica Acta, 42, 1845–1850.

Gross, G.A. (1983) Tectonic systems and the deposition of iron-formation. Precambrian Research, 20, 171–187.

Guilbaud, R., Poulton, S.W., Thompson, J., Husband, K.F., Zhu, M., Zhou, Y., Shields, G.A., and Lenton, T.M. (2020) Phosphorus-limited conditions in the early Neoproterozoic ocean maintained low levels of atmospheric oxygen. Nature Geoscience, 13, 296–301.

Halevy, I., Alesker, M., Schuster, E.M., Popovitz-Biro, R., and Feldman, Y. (2017) A key role for green rust in the Precambrian oceans and the genesis of iron formations. Nature Geoscience, 10, 135–139.

668 Halverson, G.P., Poitrasson F., Hoffman P.F., Nédélec A., Montel J.M., and Kirby J. (2011) Fe
669 isotope and trace element geochemistry of the Neoproterozoic Syn-glacial Rapitan iron
670 formation. Earth and Planetary Science Letters, 309, 300–112.
671 Han, T.M. (1978) Microstructures of magnetite as guides to its origin in some Precambrian iron-
672 formations. Fortschritte der Mineralogie, 56, 105–142.
673 ——— (1982) Iron formations of Precambrian age: Hematite-magnetite relationships in some
674 Proterozoic iron deposits—A microscopic observation. In Ore Genesis, 451–459 p. Berlin,
675 Heidelberg.
676 Han, C., Xiao, W., Su, B., Sakyi, P.A., Ao, S., Zhang, J., and Ding, J. (2017) Neoarchean
677 Algoma-type banded iron formation from the Northern Shanxi, the Trans-North China
678 Orogen: SIMS U-Pb age, origin and tectonic setting. Precambrian Research, 303, 548–572.
679 Hansen, H., and Poulsen, I.F. (1999) Interaction of synthetic sulphate “green rust” with
680 phosphate and the crystallization of vivianite. Clays and Clay Minerals, 47, 312–318.
681 Heider, F., Dunlop, D.J., and Sugiura, N. (1987) Magnetic properties of hydrothermally
682 recrystallized magnetite crystals. Science, 236, 1287–1290.
683 Heimann, A., Johnson, C.M., Beard, B.L., Valley, J.W., Roden, E.E., Spicuzza, M.J., and Beukes,
684 N.J. (2010) Fe, C and O isotope compositions of banded iron formation carbonates
685 demonstrate a major role for dissimilatory iron reduction in ~2.5 Ga marine environments.
686 Earth and Planetary Science Letters, 294, 8–18.
687 Isley, A.E., and Abbott, D.H. (1999) Plume-related mafic volcanism and the deposition of banded
688 iron formation. Journal of Geophysical Research: Solid Earth, 104, 15461–15477.
689 Jiao, Y., Kappler, A., Croal, L.R., and Newman, D.K. (2005) Isolation and Characterization of a
690 Genetically Tractable Photoautotrophic Fe(II)-Oxidizing Bacterium, Rhodopseudomonas

palustris Strain TIE-1. Applied and Environmental Microbiology, 71, 4487–4496.

Johnson, C.M., Beard, B.L., Beukes, N.J., Klein, C., and O'Leary, J.M. (2003) Ancient geochemical cycling in the Earth as inferred from Fe isotope studies of banded iron formations from the Transvaal craton. Contributions to Mineralogy and Petrology, 144, 523–547.

Johnson, C.M., Beard, B.L., Klein, C., Beukes, N.J., and Roden, E.E. (2008a) Iron isotopes constrain biologic and abiologic processes in banded iron formation genesis. Geochimica et Cosmochimica Acta, 72, 151–169.

Johnson, C.M., Beard, B.L., and Roden, E.E. (2008b) The iron isotope fingerprints of redox and biogeochemical cycling in modern and ancient earth. Annual Review of Earth and Planetary Sciences, 36, 457–493.

Kappler, A., Pasquero, C., Konhauser, K.O., and Newman, D.K. (2005) Deposition of banded iron formations by anoxygenic phototrophic Fe (II)-oxidizing bacteria. Geology, 33, 865–868.

Kaufman, A.J. (1996) Geochemical and mineralogic effects of contact metamorphism on banded iron-formation: an example from the Transvaal Basin, South Africa. Precambrian Research, 79, 171–194.

Klein, C. (2005) Some Precambrian banded iron-formations (BIFs) from around the world: Their age, geologic setting, mineralogy, metamorphism, geochemistry, and origins. American Mineralogist, 90, 1473–1499.

Klinkhammer, G., Elderfield, H., and Hudson, A. (1983) Rare earth elements in seawater near hydrothermal vents. Nature, 305, 185–188.

Koehler, M.C., Buick, R., Kipp, M.A., Stüeken, E.E., and Zaloumis, J. (2018) Transient surface

714 ocean oxygenation recorded in the ~2.66 Ga Jeerinah Formation, Australia. Proceedings of
715 the National Academy of Sciences, 115, 7711–7716.
716 Koeksoy, E., Sundman, A., Byrne, J.M., Lohmayer, R., Planer-Friedrich, B., Halevy, I., Kurt
717 Konhauser, K., and Kappler, A. (2019) Formation of green rust and elemental sulfur in an
718 analogue for oxygenated ferro-euxinic transition zones of Precambrian oceans. Geology, 47,
719 211–214.
720 Köhler, I., Konhauser, K.O., Papineau, D., Bekker, A., and Kappler, A. (2013) Biological carbon
721 precursor to diagenetic siderite with spherical structures in iron formations. Nature
722 Communications, 4, 1–7.
723 Konhauser, K.O., Hamade, T., Raiswell, R., Morris, R.C., Ferris, F.G., Southam, G., and Canfield,
724 D.E. (2002) Could bacteria have formed the Precambrian banded iron formations? Geology,
725 30, 1079–1082.
726 Konhauser, K.O., Newman, D.K., and Kappler, A. (2005) The potential significance of microbial
727 Fe(III) reduction during deposition of Precambrian banded iron formations. Geobiology, 3,
728 167–177.
729 Konhauser, K.O., Planavsky, N.J., Hardisty, D.S., Robbins, L.J., Warchola, T.J., Haugaard, R.,
730 Lalonde, S.V., Partin, C.A., Oonk, P.B.H., Tsikos, H., Lyons, T.W., Bekker, A., and Johnson,
731 C.M. (2017) Iron formations: a global record of Neoarchaean to Palaeoproterozoic
732 environmental history. Earth-Science Review, 172, 140–147.
733 Krapež, B., Barley, M.E., and Pickard, A.L. (2003) Hydrothermal and resedimented origins of
734 the precursor sediments to banded iron formation: sedimentological evidence from the Early
735 Palaeoproterozoic Brockman Supersequence of Western Australia. Sedimentology, 50, 979–
736 1011.

Laakso, T.A., and Schrag, D.P. (2018) Limitations on limitation. Global Biogeochemical Cycles, 32, 486–496.

Lantink, M.L., Oonk, P.B.H., Floor, G.H., Tsikos, H., and Mason, P.R.D. (2018) Fe isotopes of a 2.4 Ga hematite-rich IF constrain marine redox conditions around the GOE. Precambrian Research, 305, 218–235.

Li, Y.L. (2012) Hexagonal platelet-like magnetite as a biosignature of thermophilic iron-reducing bacteria and its applications to the exploration of the modern deep, hot biosphere and the emergence of iron-reducing bacteria in early Precambrian oceans. Astrobiology, 12, 1100–1108.

Li, S.Z., Zhao, G.C., Zhang, J., Sun, M., Zhang, G.W., and Luo, D. (2010) Deformational history of the Hengshan-Wutai-Fuping belt: implications for the evolution of the Trans-North China Orogen. Gondwana Research, 18, 611–631.

Li, Y.L., Konhauser, K.O., Cole, D.R., and Phelps, T.J. (2011) Mineral ecophysiological data provide growing evidence for microbial activity in banded-iron formations. Geology, 39, 707–710.

Li, W., Huberty, J.M., Beard, B., Kita, N.T., Valley, J.W., and Johnson, C.M. (2013a) Contrasting behaviour of oxygen and iron isotopes in banded iron formations revealed by *in situ* isotopic analysis. Earth and Planetary Science Letters, 384, 132–143.

Li, Y.L., Konhauser, K.O., Kappler, A., and Hao, X.L. (2013b) Experimental low-grade alteration of biogenic magnetite indicates microbial involvement in generation of banded iron formations. Earth and Planetary Science Letters, 361, 229–237.

Li, C., Planavsky, N.J., Love, G.D., Reinhard, C.T., Hardisty, D., Feng, L., Bates, S.M., Huang, J., Zhang, Q., Chu, X., and Lyons, T.W. (2015) Marine redox conditions in the middle

760 Proterozoic ocean and isotopic constraints on authigenic carbonate formation: insights from
761 the Chuanlinggou Formation, Yanshan Basin, North China. Geochimica et Cosmochimica
762 Acta, 150, 90–105.
763 Li, Y.L., Konhauser, K.O., and Zhai, M. (2017) The formation of magnetite in the early Archean
764 oceans. Earth and Planetary Science Letters, 466, 103–114.
765 Li, J., Menguy, N., Leroy, E., Roberts, A.P., Liu, P., and Pan, Y. (2020) Biomineralization and
766 Magnetism of Uncultured Magnetotactic Coccus Strain THC-1 With Non-chained
767 Magnetosomal Magnetite Nanoparticles. Journal of Geophysical Research: Solid Earth, in
768 press, https://doi.org/10.1029/2020JB020853.
769 Lin, Y., Tang, D., Shi, X., Zhou, X., and Huang, K. (2019) Shallow-marine ironstones formed by
770 microaerophilic iron-oxidizing bacteria in terminal Paleoproterozoic. Gondwana Research,
771 76, 1–18.
772 Ling, H.F., Chen, X., Li, D.A., Wang, D., Shields-Zhou, G.A., and Zhu, M. (2013) Cerium
773 anomaly variations in Ediacaran–earliest Cambrian carbonates from the Yangtze Gorges
774 area, South China: implications for oxygenation of coeval shallow seawater. Precambrian
775 Research, 225, 110–127.
776 Liu, A.Q., Tang, D.J., Shi, X.Y., Zhou, L.M., Zhou, X.Q., Shang, M.H., Li, Y., and Song, H.Y.
777 (2019) Growth mechanisms and environmental implications of carbonate concretions from
778 the ~1.4 Ga Xiamaling Formation, North China. Journal of Palaeogeography, 8, 285–300.
779 Lyons, T.W., Reinhard, C.T., and Planavsky, N.J. (2014) The rise of oxygen in Earth's early
780 ocean and atmosphere. Nature, 506, 307–315.
781 Matthews, A. (1976) Magnetite formation by the reduction of hematite with iron under
782 hydrothermal conditions. American Mineralogist, 61, 927–932.

783 Meldrum, F.C., Mann, S., Heywood, B.R., Frankel, R.B., and Bazylinski, D.A. (1993) Electron
784 microscopy study of magnetosomes in a cultured coccoid magnetotactic bacterium.
785 Proceedings of the Royal Society of London. Series B: Biological Sciences, 251, 231–236.
786 Men, Y., Wang, E., Fu, J., Jia, S., You, X., and He, Q. (2020) Geochemical constraints on the
787 genesis of the Ekou banded iron formation, Shanxi Province, North China. International
788 Journal of Earth Sciences, 109, 2851–2868.
789 Miot, J., Li, J., Benzerara, K., Sougrati, M.T., Ona-Nguema, G., Bernard, S., Jumas, J., Guyotbet,
790 F. (2014) Formation of single domain magnetite by green rust oxidation promoted by
791 microbial anaerobic nitrate-dependent iron oxidation. Geochimica et Cosmochimica Acta,
792 139, 327–343.
793 Morris, R.C. (1985) Genesis of iron ore in banded iron-formation by supergene and supergene-
794 metamorphic processes–a conceptual model. Handbook of Strata-Bound and Stratiform Ore
795 Deposits, 13, 73–235.
796 ——— (1993) Genetic modelling for banded iron-formation of the Hamersley Group, Pilbara
797 Craton, Western Australia. Precambrian Research, 60, 243–286.
798 Mozley, P.S. (1989) Relation between depositional environment and the elemental composition
799 of early diagenetic siderite. Geology, 17, 704–706.
800 Mücke, A., and Cabral, A.R. (2005) Redox and nonredox reactions of magnetite and hematite in
801 rocks. Geochemistry, 65(3), 271–278.
802 O'Loughlin, E.J., Gorski, C.A., Scherer, M.M., Boyanov, M.I., and Kemner, K.M. (2010) Effects
803 of Oxyanions, Natural Organic Matter, and Bacterial Cell Numbers on the Bioreduction of
804 Lepidocrocite (γ-FeOOH) and the Formation of Secondary Mineralization Products.
805 Environmental Science and Technology, 44, 4570–4576.

O'Loughlin, E.J., Gorski, C.A., and Michelle, M.S. (2015) Effects of phosphate on secondary mineral formation during the bioreduction of akaganeite (β-FeOOH): Green rust versus framboidal magnetite. Current Inorganic Chemistry (Discontinued), 5, 214–224.

Ohmoto, H. (2003) Nonredox transformations of magnetite–hematite in hydrothermal systems. Economic Geology, 98, 157–161.

Ohmoto, H., Watanabe, Y., and Kumazawa, K. (2004) Evidence from massive siderite beds for a CO_2-rich atmosphere before ~1.8 billion years ago. Nature, 429, 395–399.

Ona-Nguema, G., Abdelmoula, M., Jorand, F., Benali, O., Géhin, A., Block, J.C., and Génin, J.R. (2002) Iron(II,III) hydroxycarbonate green rust formation and stabilization from lepidocrocite bioreduction. Environmental Science and Technology, 36, 16–20.

Otake, T., Wesolowski, D.J., Anovitz, L.M., Allard, L.F. and Ohmoto, H. (2007) Experimental evidence for non-redox transformations between magnetite and hematite under H_2-rich hydrothermal conditions. Earth and Planetary Science Letters, 257, 60–70.

Pantke, C., Obst, M., Benzerara, K., Morin, G., Ona-Nguema, G. Dippon, U., and Kappler, A. (2012) Green rust formation during Fe(II) oxidation by the nitrate-reducing Acidovorax sp. strain BoFeN1. Environmental Science and Technology, 46, 1439–1446.

Pecoits, E., Gingras, M.K., Barley, M.E., Kappler, A., Posth, N.R., and Konhauser, K.O. (2009) Petrography and geochemistry of the Dales Gorge banded iron formation: paragenetic sequence, source and implications for palaeo-ocean chemistry. Precambrian Research, 172, 163–187.

Pedersen, H.D., Postma, D., Jakobsen, R., and Larsen, O. (2005) Fast transformation of iron oxyhydroxides by the catalytic action of aqueous Fe (II). Geochimica et Cosmochimica Acta, 69, 3967–3977.

829 Peng, D.F., Beysen, S., Li, Q., Sun, Y.F., and Yang, L.Y. (2010) Hydrothermal synthesis of
830 monodisperse α-Fe_2O_3 hexagonal platelets. Particuology, 8, 386–389.
831 Percak-Dennett, E.M., Beard, B.L., Xu, H., Konishi, H., Johnson, C.M., and Roden, E.E. (2011)
832 Iron isotope fractionation during microbial dissimilatory iron oxide reduction in simulated
833 Archaean seawater. Geobiology, 9, 205–220.
834 Perry E.C., Tan, F.C., and Morey, G.B. (1973) Geology and stable isotope geochemistry of the
835 Biwabik Iron Formation, northern Minnesota. Economic Geology, 68, 1110–1125.
836 Planavsky, N., Bekker, A., Rouxel, O.J., Kamber, B., Hofmann, A., Knudsen, A., and Lyons, T.W.
837 (2010) Rare earth element and yttrium compositions of Archean and Paleoproterozoic Fe
838 formations revisited: new perspectives on the significance and mechanisms of deposition.
839 Geochimica et Cosmochimica Acta, 74, 6387–6405.
840 Planavsky, N.J., Reinhard, C.T., Wang, X.L., Thomson, D., McGoldrick, P., Rainbird, R.H.,
841 Johnson, T., Fischer, W.W., and Lyons, T.W. (2014a) Low Mid-Proterozoic atmospheric
842 oxygen levels and the delayed rise of animals. Science, 346, 635–638.
843 Planavsky, N.J., Asael, D., Hofmann, A., Reinhard, C.T., Lalonde, S.V., Knudsen, A., Wang, X.,
844 Ossa, F., Pecoits, E., Smith, A.J.B., Beukes, N.J., Bekker, A., Johnson, T.M., Konhauser,
845 K.O., Lyons, T.W., and Rouxel, O.J. (2014b) Evidence for oxygenic photosynthesis half a
846 billion years before the Great Oxidation Event. Nature Geoscience, 7, 283–286.
847 Posth, N.R., Konhauser, K.O., and Kappler, A. (2013a) Microbiological processes in banded iron
848 formation deposition. Sedimentology, 60, 1733–1754.
849 Posth, N.R., Köhler, I., Swanner, E.D., Schroder, C., Wellmann, E., Binder, B., Konhauser, K.O.,
850 Neumann, U., Berthold, C., Nowak, M., and Kappler, A. (2013b) Simulating Precambrian
851 banded iron formation diagenesis. Chemical Geology, 362, 66–73.

852 Rasmussen, B., and Muhling, J.R. (2018) Making magnetite late again: Evidence for widespread
853 magnetite growth by thermal decomposition of siderite in Hamersley banded iron
854 formations. Precambrian Research, 306, 64–93.
855 Rasmussen, B., Fletcher, I.R., Bekker, A., Muhling, J.R., Gregory, C.J., and Thorne, A.M. (2012)
856 Deposition of 1.88-billion-year-old iron formations as a consequence of rapid crustal
857 growth. Nature, 484, 498–501.
858 Rasmussen, B., Meier, D.B., Krapež, B., and Muhling, J.R. (2013) Iron silicate microgranules as
859 precursor sediments to 2.5-billion-year-old banded iron formations. Geology, 41, 435–438.
860 Rasmussen, B., Krapež, B., Muhling, J.R., and Suvorova, A. (2015a) Precipitation of iron silicate
861 nanoparticles in early Precambrian oceans marks Earth's first iron age. Geology 43, 303–
862 306.
863 Rasmussen, B., Krapež, B., and Muhling, J.R. (2015b) Seafloor silicification and hardground
864 development during deposition of 2.5 Ga banded iron formations. Geology, 43, 235–238.
865 Rasmussen, B., Muhling, J.R., Suvorova, A., and Krapež, B. (2017) Greenalite precipitation
866 linked to the deposition of banded iron formations downslope from a late Archaean
867 carbonate platform. Precambrian Research, 290, 49–62.
868 Rasmussen, B., Muhling, J.R., and Fischer, W.W. (2019) Evidence from laminated chert in
869 banded iron formations for deposition by gravitational settling of iron-silicate muds.
870 Geology, 47, 167–170.
871 Raye, U., Pufahl, P.K., Kyser, T.K., Ricard, E., and Hiatt, E.E. (2015) The role of sedimentology,
872 oceanography, and alteration on the δ^{56}Fe value of the Sokoman Iron Formation, Labrador
873 Trough, Canada. Geochimica et Cosmochimica Acta, 164, 205–220.
874 Rego, E.S., Busigny, V., Lalonde, S.V., Philippot, P., Bouyon, A., Rossignol, C., and de Cássia

875 Zapparoli, A. (2021) Anoxygenic photosynthesis linked to Neoarchean iron formations in
876 Carajás (Brazil). Geobiology, in press, https://doi.org/10.1111/gbi.12438.
877 Reinhard, C.T., Planavsky, N.J., Robbins, L.J., Partin, C.A., Gill, B.C., Lalonde, S.V., Bekker, A.,
878 Konhauser, K.O., and Lyons, T.W. (2013) Proterozoic ocean redox and biogeochemical
879 stasis. Proceedings of the National Academy of Sciences, 110, 5357–5362.
880 Robbins, E.I., Kourtidou-Papadeli, C., Iberall, A.S., Nord Jr, G.L., and Sato, M. (2016) From
881 Precambrian iron-formation to terraforming Mars: the JIMES expedition to Santorini.
882 Geomicrobiology Journal, 33, 1–16.
883 Romanek, C.S., Jimenez-Lopez, C., Rodriguez Navarro, A., Sanchez-Roman, M., Sahai, N., and
884 Coleman, M. (2009) Inorganic synthesis of Fe–Ca–Mg carbonates at low temperature.
885 Geochimica et Cosmochimica Acta, 73, 5361–5376.
886 Ruby, C., Assa, R., Géhin, A., Cortot, J., Abdelmoula, M., and Génin, J.M. (2006) Green rusts
887 synthesis by coprecipitation of Fe^{II}–Fe^{III} ions and mass-balance diagram. Comptes Rendus
888 Geoscience, 338, 420–432.
889 Ruby, C., Abdelmoula, M., Naille, S., Renard, A., Khare, V., Ona-Nguema, G., Morin, G., Génin,
890 J.R. (2010) Oxidation modes and thermodynamics of Fe^{II-III} oxyhydroxycarbonate green
891 rust: Dissolution-precipitation versus *in situ* deprotonation. Geochimica et Cosmochimica
892 Acta, 74, 953–966.
893 Sawicki, J.A., Brown, D.A., and Beveridge, J. (1995) Microbial precipitation of siderite and
894 protoferrihydrite in a biofilm. The Canadian Mineralogist, 33, 1–6.
895 Schnetzler, C.C., and Philpotts, J.A. (1970) Partition coefficients of rare-earth elements between
896 igneous matrix material and rock-forming mineral phenocrysts—II. Geochimica et
897 Cosmochimica Acta, 34, 331–340.

898 Schwertmann, U., and Kämpf, N. (1985) Properties of Goethite and Hematite in Kaolinitic Soils
899 of Southern and Central Brazil. Soil Science, 139, 344–350.
900 Sholkovitz, E.R., and Schneider, D.L. (1991) Cerium redox cycles and rare earth elements in the
901 Sargasso Sea. Geochimica et Cosmochimica Acta, 55, 2737–2743.
902 Simonson, B.M. (1985) Sedimentological constraints on the origins of Precambrian iron-
903 formations. Geological Society of America Bulletin, 96, 244–252.
904 Simonson, B.M., Chan, M.A., and Archer, A.W. (2003) Origin and evolution of large
905 Precambrian iron formations. Special Papers Geological Society of America, 231–244.
906 Stumm, W., and Lee, G.F. (1961) Oxygenation of ferrous iron. Industrial and Engineering
907 Chemistry, 53, 143–146.
908 Sumoondur, A., Shaw, S., Ahmed, I., and Benning, L.G. (2008) Green rust as a precursor for
909 magnetite: an *in situ* synchrotron based study. Mineralogical Magazine, 72, 201–204.
910 Sun, S., and Li, Y.L. (2017) Geneses and evolutions of iron-bearing minerals in banded iron
911 formations of >3760 to ca. 2200 million-year-old: constraints from electron microscopic, X-
912 ray diffraction and Mossbauer spectroscopic investigations. Precambrian Research, 289, 1–
913 17.
914 Sun, S., Konhauser, K.O., Kappler, A., and Li, Y.L. (2015) Primary hematite in Neoarchean to
915 Paleoproterozoic oceans. Geological Society of America Bulletin, 127, 850–861.
916 Sylvestre, G., Laure, T.N.E., Djibril, K.N.G., Arlette, D.S., Cyriel, M., Timoleon, N., and Paul,
917 N.J. (2017) A mixed seawater and hydrothermal origin of Superior-type banded iron
918 formation (BIF)-hosted Kouambo iron deposit, Palaeoproterozoic Nyong series,
919 Southwestern Cameroon: constraints from petrography and geochemistry. Ore Geology
920 Reviews, 80, 860–875.

921 Tang, D., Shi, X., Wang, X., and Jiang, G. (2016) Extremely low oxygen concentration in mid-
922 Proterozoic shallow seawaters. Precambrian Research, 276, 145–157.
923 Tang, D., Shi, X., Jiang, G., Wu, T., Ma, J., and Zhou, X. (2018) Stratiform siderites from the
924 Mesoproterozoic Xiamaling Formation in North China: Genesis and environmental
925 implications. Gondwana Research, 58, 1–15.
926 Tang, D., Ma, J., Shi, X., Lechte, M., and Zhou, X. (2020) The formation of marine red beds and
927 iron cycling on the Mesoproterozoic north china platform. American Mineralogist, 105,
928 1412–1423.
929 Tian, Y.Q. (1991) Geology and Mineralization of the Wutai-Hengshan Greenstone Belt, 152 p.
930 Shanxi Science and Technology Press, Taiyuan, China, (in Chinese).
931 Tice, M.M., and Lowe, D.R. (2004) Photosynthetic microbial mats in the 3,416 Myr-old ocean.
932 Nature, 431, 549–552.
933 Tosca, N.J., Guggenheim, S., and Pufahl, P.K. (2016) An authigenic origin for Precambrian
934 greenalite: Implications for iron formation and the chemistry of ancient seawater. Bulletin,
935 128, 511–530.
936 Trendall, A.F. (2002) The significance of iron-formation in the Precambrian stratigraphic record.
937 Precambrian sedimentary environments: A modern approach to ancient depositional systems,
938 33–66, https://doi.org/10.1002/9781444304312.ch3.
939 Trower, E.J., and Lowe, D.R. (2016) Sedimentology of the 3.3 Ga upper Mendon Formation,
940 Barberton Greenstone Belt, South Africa. Precambrian Research, 281, 473–494.
941 Usman, M., Abdelmoula, M., Hanna, K., Grégoire, B., Faure, P., and Ruby, C. (2012a) Fe^{II}
942 induced mineralogical transformations of ferric oxyhydroxides into magnetite of variable
943 stoichiometry and morphology. Journal of Solid State Chemistry, 194, 328–335.

944 Usman, M., Hanna, K., Abdelmoula, M., Zegeye, A., Faure, P., and Ruby, C. (2012b) Formation
945 of green rust via mineralogical transformation of ferric oxides (ferrihydrite, goethite and
946 hematite). Applied Clay Science, 64 38–43.
947 Usman, M., Byrne, J.M., Chaudhary, A., Orsetti, S., Hanna, K., Ruby, C., Kappler, A., and
948 Haderlein, S.B. (2018) Magnetite and green rust: synthesis, properties, and environmental
949 applications of mixed-valent iron minerals. Chemical Reviews, 118, 3251–3304.
950 Viehmann, S., Bau, M., Smith, A.J., Beukes, N.J., Dantas, E.L., and Bühn, B. (2015) The
951 reliability of ~2.9 Ga old Witwatersrand banded iron formations (South Africa) as archives
952 for Mesoarchean seawater: Evidence from REE and Nd isotope systematics. Journal of
953 African Earth Sciences, 111, 322–334.
954 Vuillemin, A., Richard, W., Kemnitz, H., Schleicher, A.M., Friese, A., Bauer, K.W., Simister, R.,
955 Nomosatryo, S., Ordoñ, Luis., Ariztegui, D., Henny, C., Crowe, S., Benning, L.G.,
956 Kallmeyer, J., Russell, J.M., Bijaksana, S., and Vogel, H. (2019) Formation of diagenetic
957 siderite in modern ferruginous sediments. Geology, 47, 540–544.
958 Wang, Z.H., Wilde, S.A., Wang, K.Y., and Yu, L.J. (2004) A MORB-arc basalt–adakite
959 association in the 2.5 Ga Wutai greenstone belt: Neoarchaean magmatism and crustal
960 growth in the North China Craton. Precambrian Research, 131, 323–343.
961 Wang, C.L., Zhang, L.C., Lan, C.Y., and Dai, Y.P. (2014) Petrology and geochemistry of the
962 Wangjiazhuang banded iron formation and associated supracrustal rocks from the Wutai
963 greenstone belt in the North China Craton: implications for their origin and tectonic setting.
964 Precambrian Research, 255, 603–626.
965 Wang, C., Ding, L., Zhang, L.Y., Kapp, P., Pullen, A., and Yue, Y.H. (2016) Petrogenesis of
966 Middle-Late Triassic volcanic rocks from the Gangdese belt, southern Lhasa terrane:

967 implications for early subduction of Neo-Tethyan oceanic lithosphere. Lithos, 262, 320–333.
968 Warke, M.R., Rocco, T.D., Zerkle, A.L., Lepland, A., Prave, A.R., Martin, A.P., Ueno, Y.,
969 Condon, D.J., and Claire, M.W. (2020) The great oxidation event preceded a
970 Paleoproterozoic “snowball earth”. Proceedings of the National Academy of Sciences, 117,
971 13314–13320.
972 Webb, G.E., and Kamber, B.S. (2000) Rare earth elements in Holocene reefal microbialites: a
973 new shallow seawater proxy. Geochimica et Cosmochimica Acta, 64, 1557–1565.
974 Wiesli, R.A., Beard, B.L., and Johnson, C.M. (2004) Experimental determination of Fe isotope
975 fractionation between aqueous Fe(II), siderite and green rust in abiotic systems. Chemical
976 Geology, 211, 343–362.
977 Wilde, S.A., Cawood, P.A., Wang, K.Y., Nemchin, A.A., and Zhao, G.C. (2004) Determining
978 Precambrian crustal evolution in China: a case-study from Wutaishan, Shanxi Province,
979 demonstrating the application of precise SHRIMP U-Pb geochronology. Geological Society
980 of London, 226, 5–25.
981 Wilde, S.A., Cawood, P.A., Wang, K.Y., and Nemchin, A.A. (2005) Granitoid evolution in the
982 Late Archaean Wutai Complex, North China Craton. Journal of Asian Earth Sciences, 24,
983 597–613.
984 Wittkop, C., Teranes, J., Lubenow, B., and Dean, W.E. (2014) Carbon-and oxygen-stable isotopic
985 signatures of methanogenesis, temperature, and water column stratification in Holocene
986 siderite varves. Chemical Geology, 389, 153–166.
987 Wu, C.H., and Zhong, C.T. (1998) The Paleoproterozoic SW-NE collision model for the central
988 North China Craton. Progress in Precambrian Research, 21, 28–50 (in Chinese).
989 Xie, B.Z., Sun, L.F., Fang, H., Shi, X.Y, and Tang, D.J. (2021) Siderite in banded iron formation

990 from Neoarchean Baizhiyan Formation, Shanxi Province: genesis and paleoenvironmental
991 implications. Journal of Palaeogeography, 23, 175–190. (in Chinese with English abstract)
992 Zegeye, A., Mustin, C., and Jorand, F. (2010) Bacterial and iron oxide aggregates mediate
993 secondary iron mineral formation: green rust versus magnetite. Geobiology, 8, 209–222.
994 Zegeye, A., Bonneville, S., Benning, L.G., Sturm, A., Fowle, D.A., Jones, C., Canfield, D.E.,
995 Ruby, C., Maclean, L.C., Nomosatryo, S., Crowe, Sean., and Poulton, S.W. (2012) Green
996 rust formation controls nutrient availability in a ferruginous water column. Geology, 40,
997 599–602.
998 Zhao, G., Sun, M., Wilde, S.A., and Li, S.Z. (2005) Late Archean to Paleoproterozoic evolution
999 of the North China Craton: key issues revisited. Precambrian Research, 136, 177–202.
1000 Zheng, X.Y., Beard, B.L., Reddy, T.R., Roden, E.E., and Johnson, C.M. (2016) Abiologic silicon
1001 isotope fractionation between aqueous Si and Fe (III)–Si gel in simulated Archean seawater:
1002 Implications for Si isotope records in Precambrian sedimentary rocks. Geochimica et
1003 Cosmochimica Acta, 187, 102–122.
1004 Zhou, L.M., Wang, R., Hou, Z.Q., Li, C., Zhao, H., Li, X.W., and Qu, W.J. (2018) Hot
1005 Paleocene-Eocene Gangdese arc: Growth of continental crust in southern Tibet. Gondwana
1006 Research, 62, 178–197.
1007

Figure Captions

Figure 1. Geological setting. (**a**) Tectonic subdivision of the North China Craton (modified after Zhao et al. 2005). (**b**) Regional geological sketch showing location of the Hengshan–Wutai–Fuping belt in the North China Craton (after Zhao et al. 2005). (**c**) Simplified geological map showing the study area (modified after the 1:250,000 Geological Map of China, the China Geological Survey 2013).

Figure 2. Stratigraphic column showing group and formation subdivisions for various rock assemblages in the Wutai greenstone belt (modified after Han et al. 2017).

Figure 3. Macroscopic and microscopic features of the BIFs from the Baizhiyan Formation, Shanxi, China. (**a**) BIF with alternated wavy iron-rich (Mag) and silica-rich bands (Qz). (**b**) BIF with alternated wavy iron-rich (Mag) and silica-rich bands (Qz). (**c**) Polished BIF slab showing BIF clasts in well-preserved iron-rich (Mag) and silica-rich bands (Qz). (**d**) BIF with straight iron- (Mag) and silica-rich (Qz) bands, and the iron rich bands showing thinner lamination structure. (**e**) A siderite layer interbeded in the iron-rich bands. (**f**) A BSE image showing detrital particle supported by the siderite matrix; Mag = magnetite, Qz =quartz, Sd = siderite.

Figure 4. Microscopic features of the Baizhiyan BIFs. (**a**) A BSE image with low magnification, showing alternating iron-rich and silica-rich bands; the iron-rich band consisting of magnetite (Mag) with some ankerite (Ank), while the silica-rich band dominated by quartz (Qz), with minor magnetite and siderite. (**b**) Close view of silica-rich band (Qz), showing small magnetite (Mag) and siderite (Sd) crystals in the band. (**c**) An euhedral hexagonal magnetite (Mag) crystal,

contacted with quartz (Qz) and siderite (Sd). (**d**) An EDS spectrum and quantitative analysis result of the magnetite in panel c. (**e**) Electron backscattered diffraction analysis of the hexagonal magnetite in panel c. (**f**)–(**h**) hexagonal magnetite (Mag) crystals with variable size from ~3 μm to ~30 μm, Qz =quartz, Sd = siderite.

Figure 5. X-ray diffraction results of the Baizhiyan BIFs. (**a**) X-ray diffraction patterns of silica-rich bands, showing that they are mainly composed of quartz, with minor amount of magnetite, siderite, ankerite and chamosite. (**b**) X-ray diffraction patterns of iron-rich bands, showing that they are mainly composed of magnetite with minor quartz, ankerite, siderite and chamosite.

Figure 6. Cross-plot of TFe_2O_3 versus P_2O_5 contents, showing their positive correlation.

Figure 7. REE+Y patterns of the Baizhiyan BIFs. (**a**) REE+Y pattern of iron-rich bands, showing light-REE-depleted pattern with prominent positive Eu anomalies and none to slightly positive Ce anomalies. (**b**) REE+Y pattern of screened iron-rich band samples with Y/Ho > 32 and $Pr_{SN}/Yb_{SN} < 0.5$. (**c**) REE+Y pattern of silica-rich bands, showing light-REE-depleted pattern with prominent positive Eu anomalies and none to slightly positive Ce anomalies. (**d**) REE+Y pattern of screened silica-rich band samples with Y/Ho > 32 and $Pr_{SN}/Yb_{SN} < 0.5$.

Figure 8. Geochemical features of the Baizhiyan BIFs. (**a**) Cross-plot of Th versus ΣREE. (**b**) Cross-plot of Th versus Y/Ho. (**c**) Cross-plot of Th versus $Pr_{SN/}Yb_{SN.}$ (**d**) Cross-plot of ΣREE versus Ce_{SN}/Ce_{SN}*. (**e**) Cross-plot of Th versus Ce_{SN}/Ce_{SN}*. (**f**) Cross-plot of Th versus Eu_{SN}/Eu_{SN}*.

Figure 9. A schematic showing magnetite formed in Archean ferruginous seawater with different origins of green rust as intermediate product (modified from Halevy et al. 2017; Li et al. 2017; Lin et al. 2019).

TABLE S1. XRD analysis result of the Baizhiyan BIFs

TABLE S2. Major element contents (wt%) of the Baizhiyan BIFs

TABLE S3. Trace element concentrations of the Baizhiyan BIFs (μg/g) and related redox proxies

This is the peer-reviewed, final accepted version for American Mineralogist, published by the Mineralogical Society of America.
The published version is subject to change. Cite as Authors (Year) Title. American Mineralogist, in press.
DOI: https://doi.org/10.2138/am-2022-7981. http://www.minsocam.org/

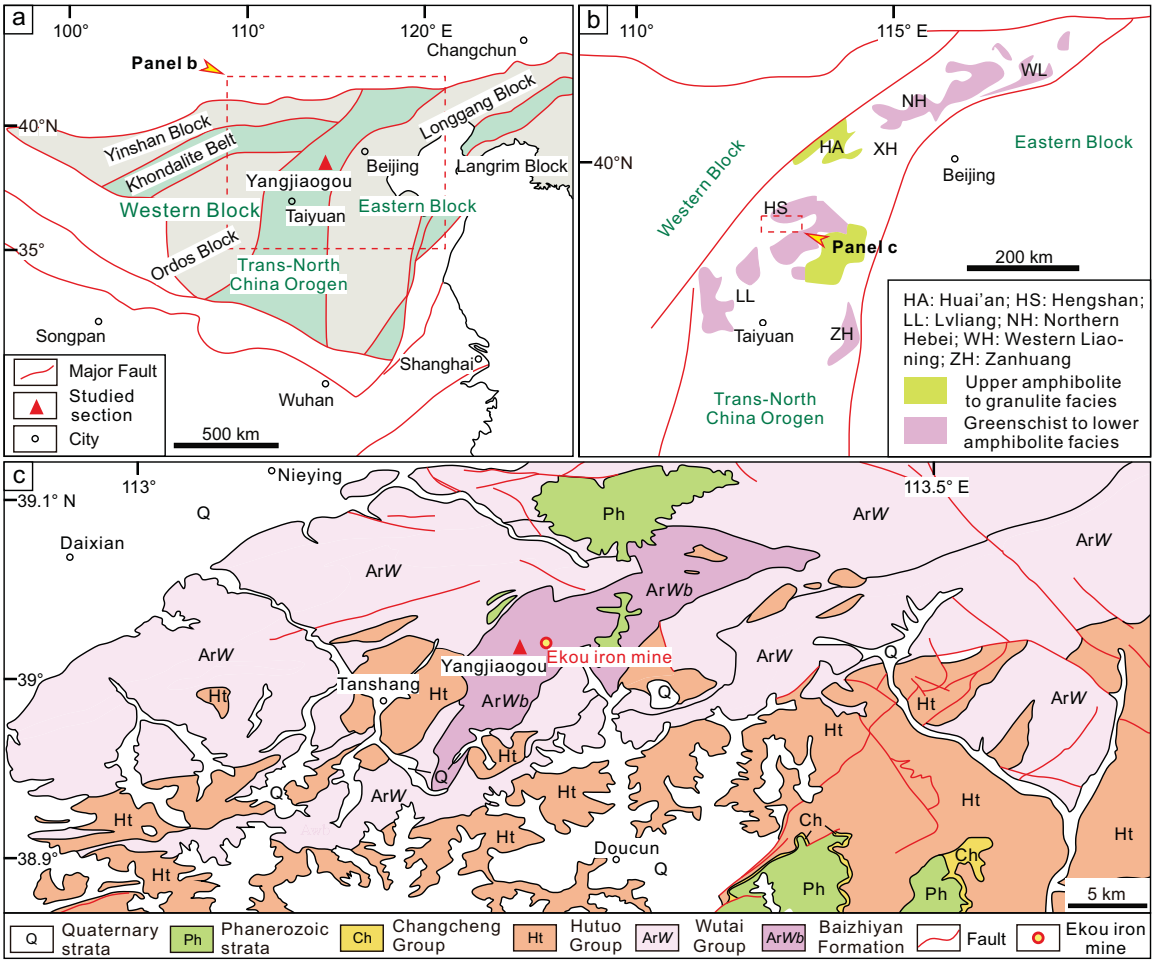

Figure 1

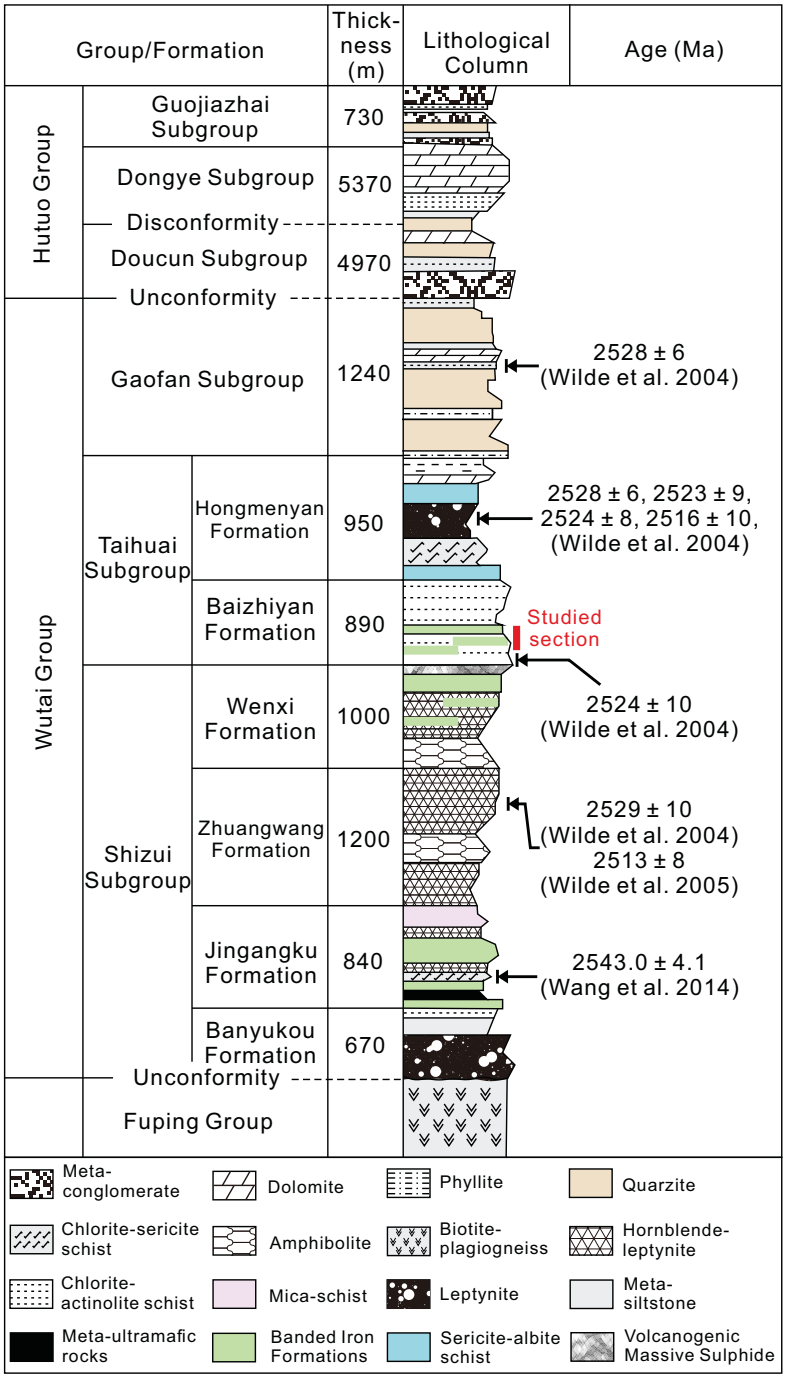

Figure 2

This is the peer-reviewed, final accepted version for American Mineralogist, published by the Mineralogical Society of America.
The published version is subject to change. Cite as Authors (Year) Title. American Mineralogist, in press.
DOI: https://doi.org/10.2138/am-2022-7981. http://www.minsocam.org/

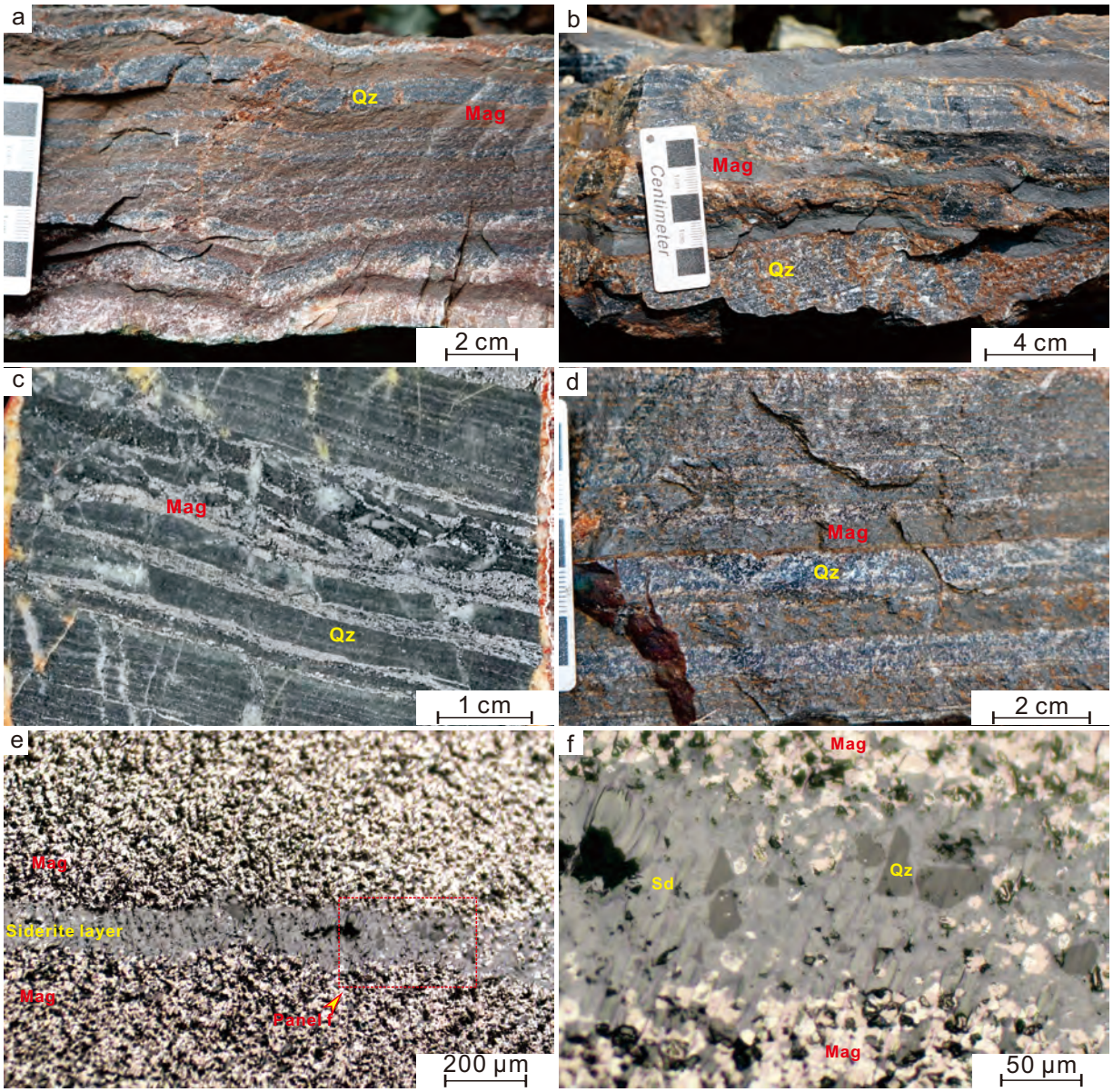

Figure 3

This is the peer-reviewed, final accepted version for American Mineralogist, published by the Mineralogical Society of America.
The published version is subject to change. Cite as Authors (Year) Title. American Mineralogist, in press.
DOI: https://doi.org/10.2138/am-2022-7981. http://www.minsocam.org/

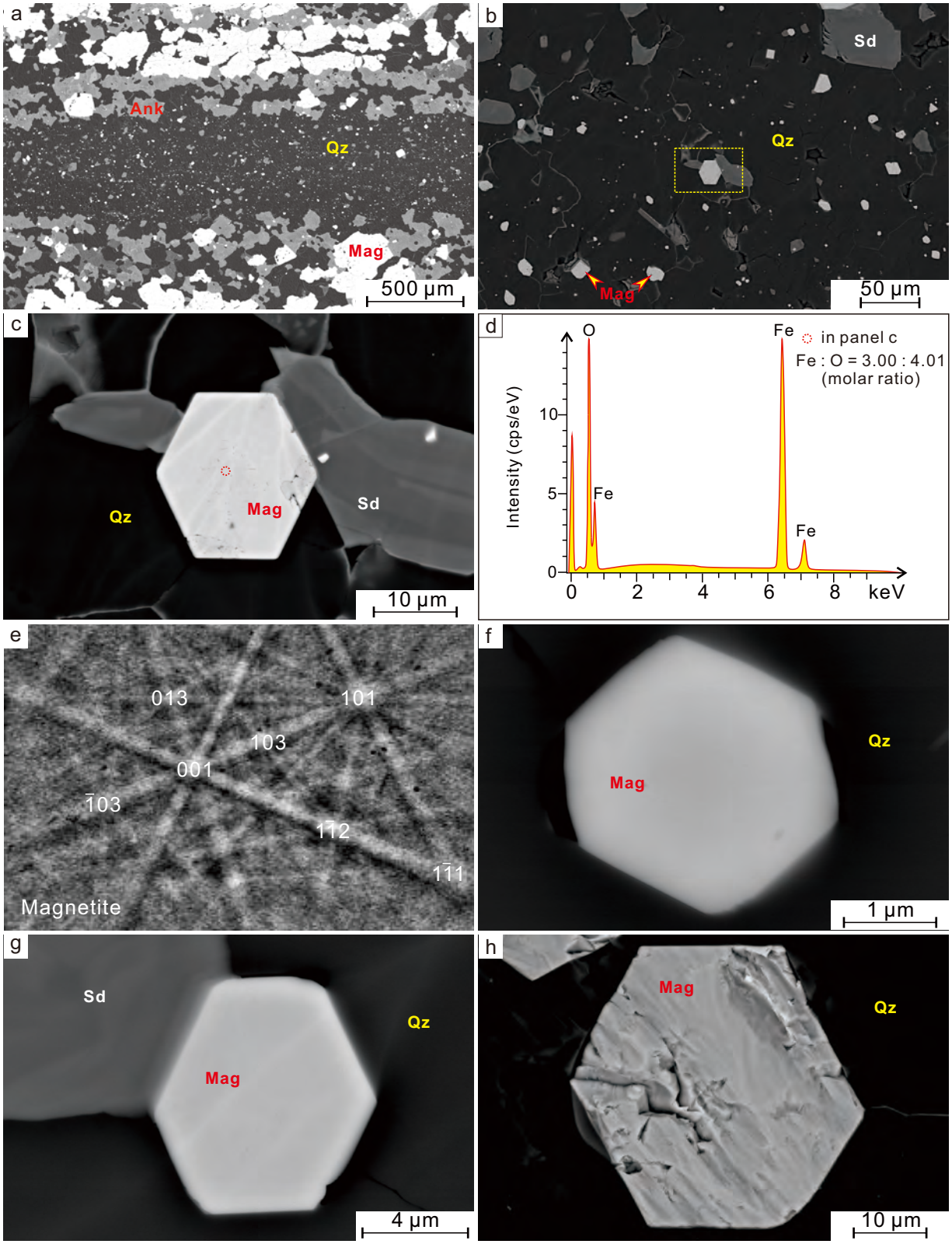

Figure 4

This is the peer-reviewed, final accepted version for American Mineralogist, published by the Mineralogical Society of America.
The published version is subject to change. Cite as Authors (Year) Title. American Mineralogist, in press.
DOI: https://doi.org/10.2138/am-2022-7981. http://www.minsocam.org/

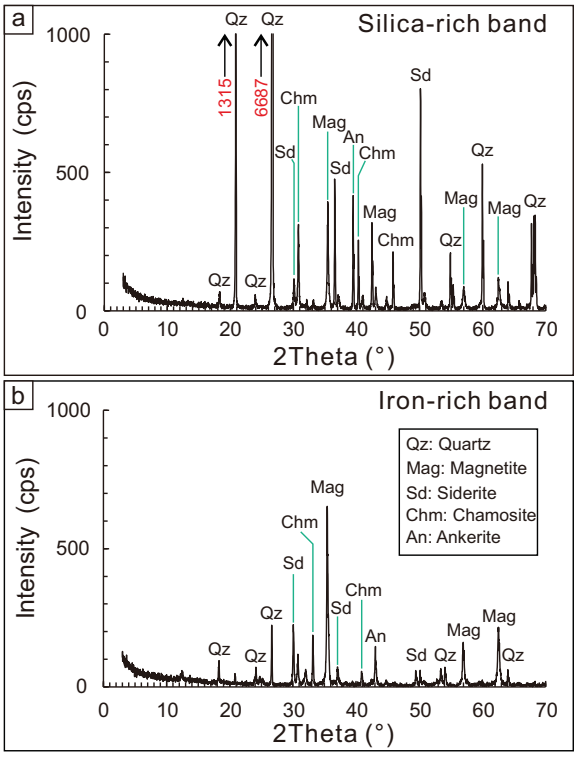

Figure 5

This is the peer-reviewed, final accepted version for American Mineralogist, published by the Mineralogical Society of America.
The published version is subject to change. Cite as Authors (Year) Title. American Mineralogist, in press.
DOI: https://doi.org/10.2138/am-2022-7981. http://www.minsocam.org/

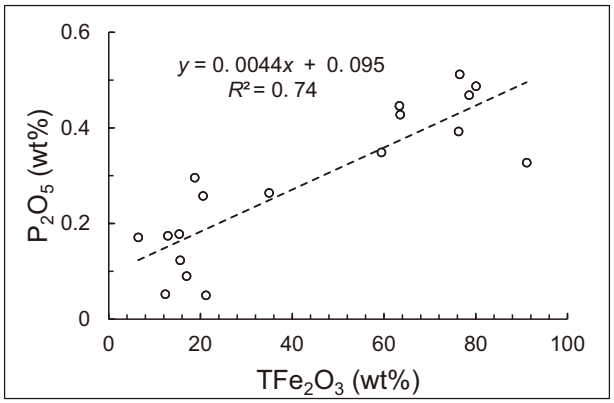

Figure 6

This is the peer-reviewed, final accepted version for American Mineralogist, published by the Mineralogical Society of America.
The published version is subject to change. Cite as Authors (Year) Title. American Mineralogist, in press.
DOI: https://doi.org/10.2138/am-2022-7981. http://www.minsocam.org/

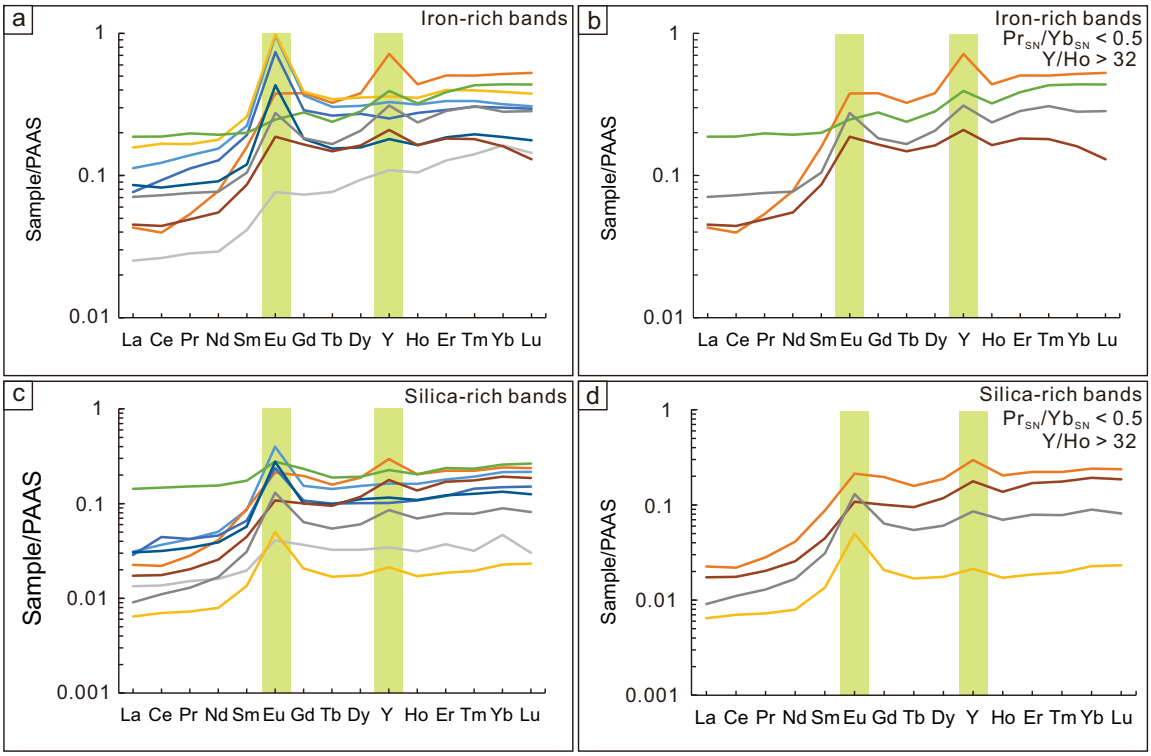

Figure 7

This is the peer-reviewed, final accepted version for American Mineralogist, published by the Mineralogical Society of America.
The published version is subject to change. Cite as Authors (Year) Title. American Mineralogist, in press.
DOI: https://doi.org/10.2138/am-2022-7981. http://www.minsocam.org/

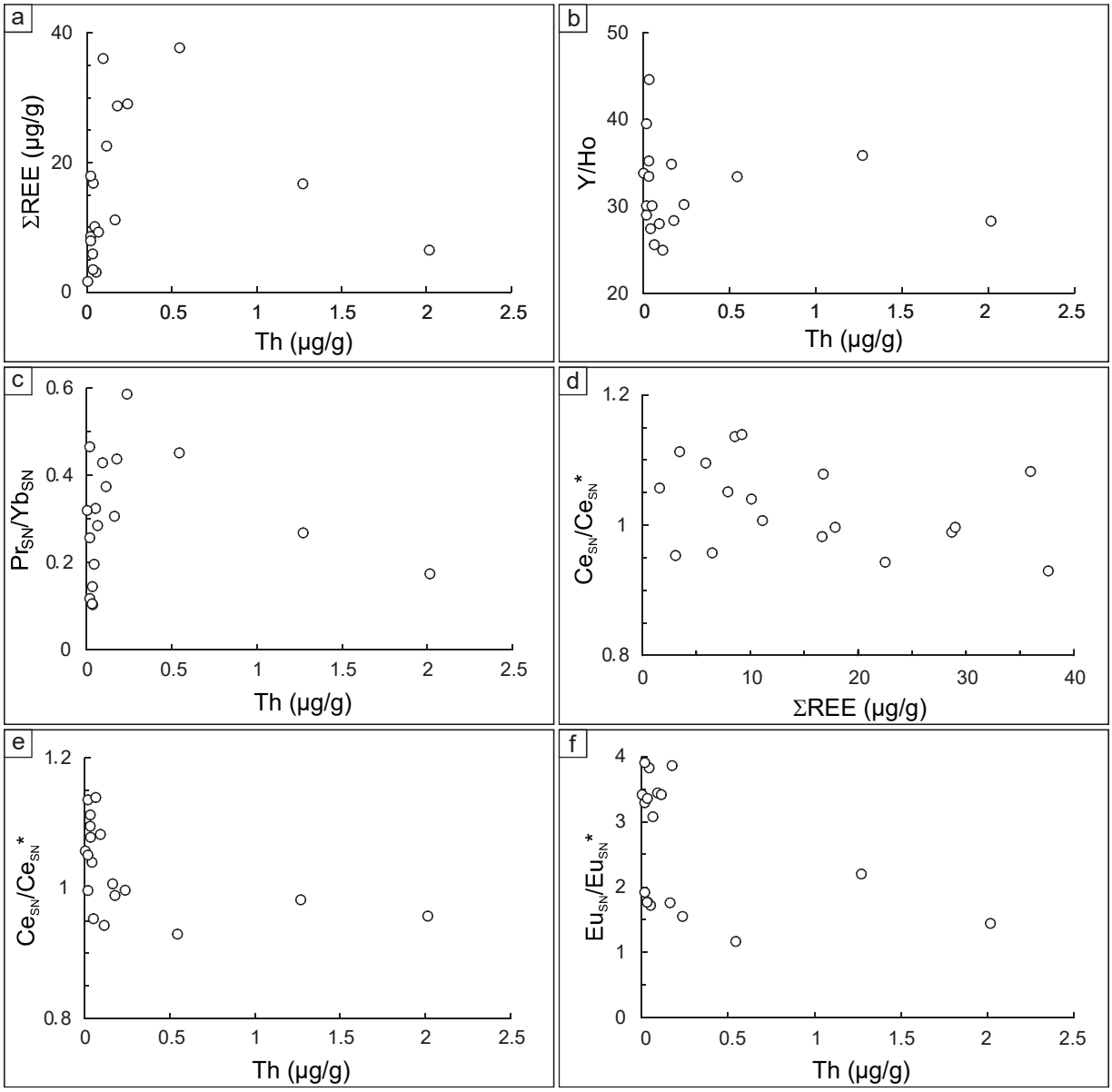

Figure 8

This is the peer-reviewed, final accepted version for American Mineralogist, published by the Mineralogical Society of America.
The published version is subject to change. Cite as Authors (Year) Title. American Mineralogist, in press.
DOI: https://doi.org/10.2138/am-2022-7981. http://www.minsocam.org/

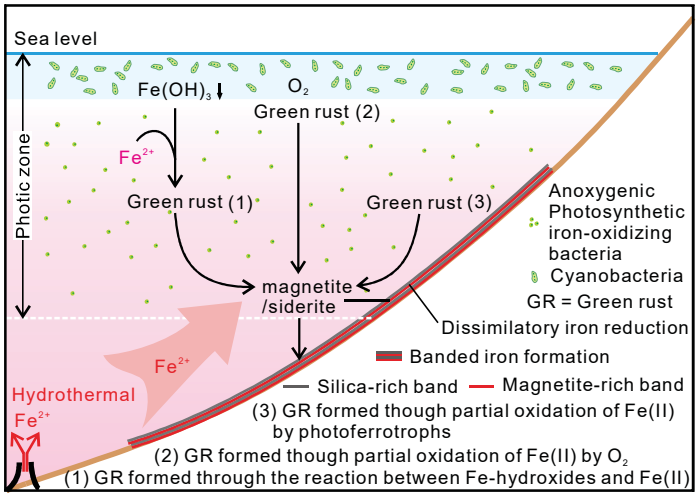

Figure 9